Superfluid helium quantum interference devices: physics and applications

Y Sato[1] and R E Packard[2]

[1] Rowland Institute at Harvard, Harvard University, Cambridge, MA 02142, USA
[2] Department of Physics, University of California at Berkeley, Berkeley, CA 94720, USA

E-mail: sato@rowland.harvard.edu and rpackard@berkeley.edu

Abstract
We present an overview of recent developments related to superfluid helium quantum
interference devices (SHeQUIDs). We discuss the physics of two reservoirs of superfluid
helium coupled together and describe the quantum oscillations that result from varying the
coupling strength. We explain the principles behind SHeQUIDs that can be built based on
these oscillations and review some techniques and applications.

(Some figures may appear in colour only in the online journal)

Contents

1. Introduction

Macroscopic quantum systems such as superconductors, superfluids and Bose–Einstein condensed gases exhibit Josephson oscillations between two samples weakly coupled together [1]. The oscillations are driven when a chemical potential difference $\Delta\mu$ is applied across the weak link and the resultant Josephson frequency is given by

$$f_J = \frac{\Delta\mu}{h}, \qquad (1)$$

where h is Planck's constant. These phenomena can be exploited in interferometer devices. The widely used SQUID [2] (superconducting quantum interference device) is the best known of these devices. This paper focuses on the recently developed superfluid helium quantum interference device (SHeQUID).

We begin by explaining the SHeQUID principle and follow by describing the physics of the Josephson oscillations that lie at the heart of the technology. We then return to discuss various related SHeQUID techniques that enhance the utility of the devices. The appendices contain several related topics.

2. SHeQUID principles

In this section, we discuss how superfluid weak-link Josephson oscillations can be used to construct a novel helium quantum interferometer. For the benefit of this discussion we must assume for the moment that these oscillations exist. The following discussion will detail the weak-coupling physics and the oscillation phenomenon itself.

To illustrate the basic principle behind superfluid quantum interference, we will first focus on the double-path configuration: see figure 1. A torus filled with superfluid helium (specifically ^{4}He or ^{3}He–B) is interrupted by two weak links. Superfluids are described by an order parameter (often called a wavefunction) containing a complex phase factor: $e^{i\phi}$ where the phase ϕ varies in space and is related to the superfluid velocity by the formula [3]

$$v_s = \frac{\hbar}{m}\nabla\phi. \qquad (2)$$

Here m is the atomic mass of the superfluid's constituent particles (i.e. ^{4}He atoms or two ^{3}He atoms). When a constant chemical potential difference is established across these junctions, one weak link oscillates as $I_{c,1}\sin(\omega_J t)$ and the other as $I_{c,2}\sin(\omega_J t + \Delta\phi_{ext})$, where $I_{c,1}$ and $I_{c,2}$ are the oscillation amplitudes, $\omega_J = 2\pi f_J$ is the Josephson frequency, and $\Delta\phi_{ext}$ is the phase shift between the two oscillations. The total current is a sum of the two oscillations, which can be written as

$$I = I_{c,1}\sin(\omega_J t) + I_{c,2}\sin(\omega_J t + \Delta\phi_{ext}) = I_c^*\sin(\omega_J t), \qquad (3)$$

where

$$I_c^* = (I_{c,1} + I_{c,2})\sqrt{\cos^2(\Delta\phi_{ext}/2) + \gamma^2\sin^2(\Delta\phi_{ext}/2)} \qquad (4)$$

with $\gamma = (I_{c,1} - I_{c,2})/(I_{c,1} + I_{c,2})$. The overall oscillation amplitude I_c^* is now a function of the external phase shift $\Delta\phi_{ext}$. This is analogous to a superconducting quantum interference device (dc-SQUID), where a similar argument leads to electrical current oscillation with amplitude modulated with external magnetic flux. In the superfluid helium case, two complex order parameters (the so-called wavefunctions) describing the neutral system interfere so that the total mass-current oscillation amplitude modulates with varying external phase shift. The device is then an interferometer. In the simplest case of $I_{c,1} = I_{c,2}$, I_c^* reduces to $2I_{c,1}|\cos(\Delta\phi_{ext}/2)|$.

Two essential elements of the device are that the oscillations exist and that the phase difference can be induced as a function of external influences of interest. We will describe
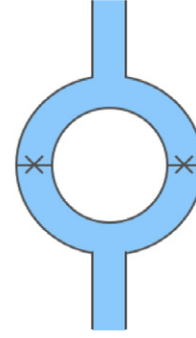

Figure 1. Superfluid interferometer. Two junctions (indicated by crosses) are placed in a superfluid torus as in the case of a dc-SQUID.

the nature of these oscillations in the next section and then discuss how certain physical interactions give rise to phase shifts between two weak links when configured as in figure 1.

3. Weakly coupled quantum fluids

3.1. Josephson equations

A superfluid such as ^{4}He or ^{3}He–B is described by the Landau two-fluid model [4] augmented by a macroscopic wavefunction $\Psi = \sqrt{\rho_s}e^{i\phi}$, where ρ_s is the superfluid density and ϕ, the quantum mechanical phase, is a rescaled velocity potential for the superfluid velocity as shown in (2). The wavefunction is properly normalized with the condensate mass density. The phase and current equations to appear later in the paper involve the superfluid mass density appropriately, but this distinction is ignored in the simple heuristic model here.

Consider the situation depicted in figure 2. Two superfluid reservoirs are linked at a junction labelled X. If the coupling between the two reservoirs is sufficiently weak, the two superfluids are described by wavefunctions, $\Psi_L = \sqrt{\rho_{s,L}}e^{i\phi_L}$ and $\Psi_R = \sqrt{\rho_{s,R}}e^{i\phi_R}$. The time-dependent Schrödinger equation $(i\hbar\partial\Psi/\partial t = \hat{H}\Psi)$ applied to this coupled system gives [5, 6]

$$i\hbar\frac{\partial\Psi_L}{\partial t} = \mu_L\Psi_L + \hbar\chi\Psi_R \qquad (5)$$

and

$$i\hbar\frac{\partial\Psi_R}{\partial t} = \mu_R\Psi_R + \hbar\chi\Psi_L, \qquad (6)$$

where μ_L and μ_R represent the chemical potentials of the two reservoirs and $\hbar\chi$ represents the effect of coupling across the junction. Here, χ has the dimension of frequency, and it gives a measure of Ψ_L leaking into Ψ_R and vice versa. The chemical potentials μ_L and μ_R are the energies required to bring one additional constituent particle from infinity to the respective reservoirs. Inserting Ψ_L and Ψ_R into (5) and (6), one obtains two equations:

$$\frac{\partial\rho_{s,L}}{\partial t} = -\frac{\partial\rho_{s,R}}{\partial t} = 2\chi\sqrt{\rho_{s,L}\rho_{s,R}}\sin(\phi_R - \phi_L) \qquad (7)$$

and

$$\frac{\partial}{\partial t}(\phi_R - \phi_L) = -\frac{1}{\hbar}(\mu_R - \mu_L). \qquad (8)$$

A mass current, I, between the two reservoirs is proportional to the $\partial\rho_s/\partial t$ terms in (7). By defining the phase
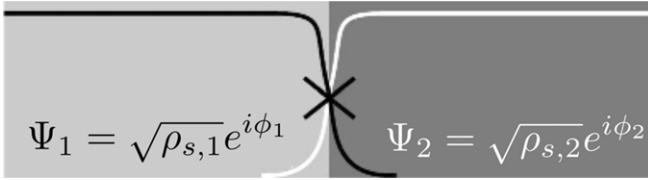
Figure 2. A schematic view of the overlapping wavefunctions.

difference $\Delta\phi = \phi_R - \phi_L$ and the chemical potential difference $\Delta\mu = \mu_R - \mu_L$, one can rewrite these equations as

$$I = I_c \sin \Delta\phi \qquad (9)$$

and

$$\frac{\partial \Delta\phi}{\partial t} = -\frac{\Delta\mu}{\hbar}, \qquad (10)$$

where I_c is proportional to the coupling strength χ. These equations were first encountered by Josephson in the context of superconducting tunnelling through a thin insulator [1]. Equation (9) is often called the dc-Josephson equation (or the Josephson current-phase relation) and applies only to weakly coupled quantum systems. On the other hand, equation (10), often called the phase-evolution equation, is much more general [7, 8]. Equation (10) is generally applicable to the time evolution of phase difference between any two locations in superfluids, superconductors and Bose–Einstein condensates whether weakly coupled or not. In essence, it is a statement of Newton's law of motion cloaked via (2) in quantum symbolism.

Equations (9) and (10) predict a striking phenomenon. If a fixed chemical potential difference is established between two weakly coupled superfluids, (10) implies that the phase difference increases linearly in time as $\Delta\phi = -(\Delta\mu/\hbar)t$. Inserting this result into (9) immediately leads to the prediction that a constant dc chemical potential difference (e.g. a fixed force pushing superfluid from one side toward the other) should (counter-intuitively) produce an oscillating mass current:

$$I = I_c \sin (\Delta\mu/\hbar)t. \qquad (11)$$

We refer to this phenomenon as a Josephson oscillation and its frequency $f_J = \Delta\mu/h$ as the Josephson frequency (1). For the range of chemical potential differences that will be relevant here, f_J typically lies in the audio region, in marked contrast to superconductors where the typical frequency range is in the microwave region.

3.2. Weak-link criterion: the healing length

To observe Josephson oscillations described above, two macroscopic quantum systems need to be 'weakly' coupled. In superconducting Josephson junctions, this is achieved by either connecting two superconductors with a thin insulator (SIS junction [9]), a normal metal barrier (SNS junction [9]), or linking the two systems with a narrow superconducting bridge [10] whose dimension is on the order of the superconducting healing length. This healing length, ξ, is the minimum distance over which there will be an appreciable change in $|\Psi|$, and the suppressed superconductivity in that length scale acts as

the necessary weak link in the microbridge configuration. A tunnel-type connection is not feasible in a superfluid helium system because an atom is too massive to exhibit appreciable tunneling. One is then left with the option of connecting two superfluid reservoirs using a constriction/aperture whose size is comparable to the superfluid healing length.

For superfluid ^{3}He one finds (at zero ambient pressure)

$$\xi_3 = \frac{65 \, \text{nm}}{(1 - T/T_c)^{1/2}}, \qquad (12)$$

where the transition temperature $T_c = 1 \, \text{mK}$ [11]. This characteristic size came within the capability of nanofabrication techniques about 25 years ago, which corresponds to the first report of an observed $\sin\phi$ current–phase relation [12].

In contrast the healing length of ^{4}He has been found to be represented by [13]

$$\xi_4 = \frac{0.3 \, \text{nm}}{(1 - T/T_\lambda)^{0.67}}, \qquad (13)$$

where the superfluid transition temperature $T_\lambda = 2.17 \, \text{K}$ at zero ambient pressure. An aperture one atom in diameter in a wall one atom thick may be too fragile to handle. Furthermore, even if it could be incorporated into an apparatus, the mass current to be detected would be below that accessible to present technology. This is the main reason why the discovery of Josephson phenomena in superfluid ^{3}He and their application to build interference devices preceded those of superfluid ^{4}He by almost two decades.

Early evidence of $\sin\phi$ current-phase behavior in superfluid ^{4}He was presented by Sukhatme *et al* [14] followed soon after by the direct observation of Josephson oscillations by Hoskinson *et al* [15]. Their work took advantage of the growth of ξ_4 near T_λ as given in (13). This variation predicts $\xi_4 \sim 60 \, \text{nm}$ when $T_\lambda - T \sim 1 \, \text{mK}$. The ^{4}He Josephson work has progressed rapidly since then given the ease of cryogenics involved at 2 K compared with 1 mK required for superfluid ^{3}He.

3.3. Superfluid Josephson weak links

A superfluid weak link is conceptually similar to a microbridge—a narrow constriction connecting two volumes of superfluid helium. The requirement for the constriction is that the length and at least one of its transverse dimensions must be on the order of the superfluid healing length. Although the simplest geometry that satisfies this condition is a single hole, the Josephson mass current through a single aperture of healing length dimensions is too small to detect with present methods. Therefore, one needs to increase this current. One option is to employ a slit-like aperture for which only one transverse dimension is on the order of the healing length (and the other dimension much larger). Another option is to employ an array of apertures, which (hopefully) behave quantum coherently so that all apertures experience the identical instantaneous phase difference.

The former approach was pursued by Avenel and Varoquaux [12]. In their early work on ^{3}He Josephson
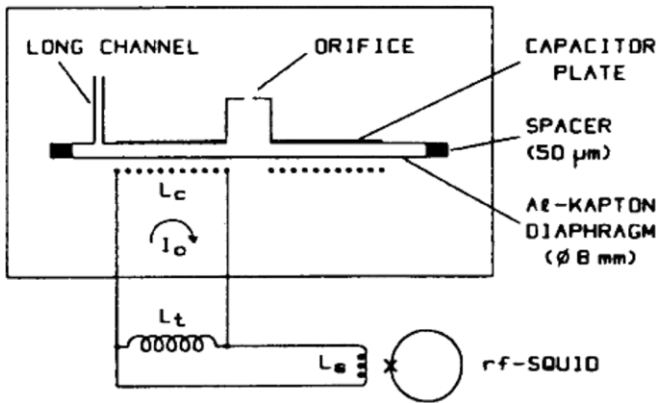
Figure 3. Experimental apparatus used for Josephson work at Saclay. Two chambers are connected through a small slit orifice and a larger parallel channel. The parallel channel shorts out dc pressure differentials but permits circulation changes in the closed path that passes through both the channel and orifice. Reprinted with permission from [17]. Copyright 1985 by the American Physical Society.

phenomenon, they used ion milling to cut a 300 nm by 5 μm slit structure in a 200 nm thick nickel foil. The latter approach (i.e. using an array of apertures) was pursued at the University of California at Berkeley, and they showed that a large array (∼4000) of apertures (square in cross section, 100 nm in size, etched in a 50 nm thick silicon nitride window) behaved quantum coherently, thus amplifying currents by the number of holes [16]. A few array types have been employed since then, first for the ^{3}He Josephson work and then for the ^{4}He equivalent. With hindsight, it might appear perfectly reasonable to have used arrays of slits or apertures to amplify the overall mass-current oscillation amplitude. However, the idea that an array will behave quantum coherently and add currents constructively to amplify the signal was not (and to some extent still not) at all obvious, especially for the ^{4}He work. This mystery of synchronicity or coherence among apertures is discussed in appendix B.

3.4. ^{3}He Josephson oscillation

The first experimental evidence for a superfluid $\sin \phi$ current–phase relation was reported for a ^{3}He system by Avenel and Varoquaux in 1988 [12]. Figure 3 shows their original apparatus configuration [17]. A slit-like weak link (300 nm by 5 μm) is used to connect two superfluid reservoirs but it is shunted by a larger tube and coupled to a diaphragm to form a hydrodynamic resonator. The diaphragm's motion is tracked with a device similar to the superconducting displacement transducer devised by Paik [18]. The diaphragm is coated with a superconducting metal. A superconducting coil containing a persistent electrical current is positioned below the diaphragm. Motion of the diaphragm (indicating fluid flow through both the tube and the orifice) changes the coil's inductance and induces changes in the persistent current flowing in the coil, which are then detected with an rf-SQUID coupled to the circuit.

Fluid flow through the two parallel flow paths can be characterized by a kinetic inductance L and the diaphragm can be represented by an effective capacitance C [19]. Therefore

the system has a hydrodynamic resonance at a frequency $1/\sqrt{LC}$. As in the superconducting Josephson inductance [9], the weak link inductance is a function of the phase difference across it: $L_{\rm J} = \kappa_3/(2\pi I_{\rm c} \cos \phi)$ where $\kappa_3 \equiv h/2m_3$ is the circulation quantum for superfluid ^{3}He. Thus the oscillator is nonlinear as a function of its amplitude. The observation of nonlinearity in the hydrodynamic resonator behavior then provides the evidence for the presence of weak-link physics.

Avenel and Varoquaux analyzed their resonator dynamics by parametrizing the relation between the mass current and the quantum phase using a model introduced by Deaver and Pierce for superconductors [20]. They assume that the slit-like aperture consists of a linear inductance in series with a purely sinusoidal one. For the latter, $I(\theta_1) = I_{\rm c} \sin \theta_1$. For the linear inductance, $I(\theta_2) = \hbar\theta_2/2m_3 L_l$. Here θ_1 is the phase difference across the sine-like element, θ_2 is the phase drop across the linear inductance L_l and $\Delta\phi = \theta_1 + \theta_2$ is the total phase drop across the combined system. The model can be characterized in terms of $I_{\rm c}$ and the ratio of two inductances $\alpha = L_1/L_{\rm J}$. Here $L_{\rm J}$ is the kinetic inductance of the ideal weak link evaluated with zero phase bias ($\theta_1 = 0$). The overall current–phase relation can be written parametrically: $I = I_{\rm c} \sin \theta_1$, $\Delta\phi = \theta_1 + \alpha \sin \theta_1$. The amplitude of the oscillator is measured as a function of driving force and frequency, and the peak amplitude of the oscillator motion is shown in figure 4. Staircase-like patterns arise from circulation changes in the closed path that passes through both the large parallel channel and a weak-link orifice. The solid line is a fit from a numerical simulation with $I_{\rm c}$ and α as fitting parameters [21]. Good fits using this model provided the first experimental evidence consistent with a Josephson-like current–phase relation. We will come back to this model in appendix A where we discuss the current–phase relation for superfluid ^{4}He.

The most striking feature of weakly coupled quantum liquids is the existence of Josephson oscillations resulting from a constant dc chemical potential difference. This was first observed in superfluid ^{3}He in 1997 [16]. For superfluid helium, chemical potential difference is given by

$$\Delta\mu = m^*(\Delta P/\rho - s\,\Delta T), \tag{14}$$

where ρ is the fluid density, s is the specific entropy, ΔP and ΔT are pressure and temperature differentials and m^* is the effective mass of superfluid constituents [3]. For superfluid ^{4}He, m^* is m_4, the atomic mass of ^{4}He. For superfluid ^{3}He, m^* equals twice the ^{3}He atomic mass due to the pairing of ^{3}He atoms. For superfluid ^{3}He at its associated temperature of ∼1 mK, the pressure term of the chemical potential difference completely dominates over the temperature term. Then the Josephson frequency relation reduces to

$$f_{\rm J} = \frac{\Delta\mu}{h} = \frac{2m_3}{\rho h}\Delta P = 187\,{\rm Hz\,mPa^{-1}}. \tag{15}$$

Establishing a pressure difference across a weak-link element should therefore cause the fluid to oscillate at a frequency proportional to the applied pressure differential.

A direct observation of such oscillations was reported by Pereversev *et al* [16] using an apparatus schematically
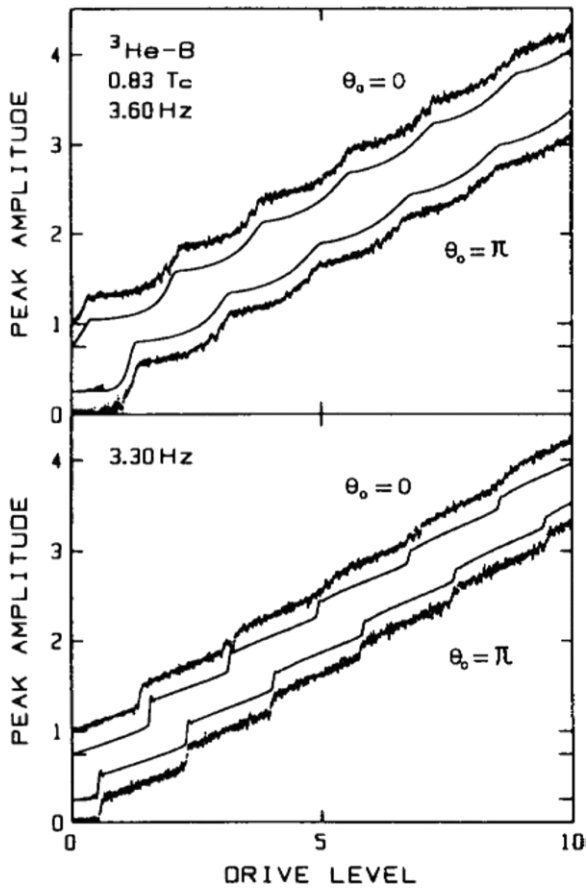
Figure 4. Observed staircase patterns in ^{3}He. Solid lines are fits using the Deaver–Pierce current-phase model. Reprinted from [21], copyright 1992 by Elsevier.

Figure 5. Experimental apparatus used for ^{3}He Josephson work at Berkeley. Two reservoirs of superfluid helium are coupled through a weak-link junction. Reprinted by permission from Macmillan Publishers Ltd: *Nature* [16], copyright 1997.

shown in figure 5. The experimental cell consists of a cylindrical container bounded on top and bottom by flexible membranes. Both membranes are metal coated, the top one with a superconducting film and the bottom one with a normal metal. Electrodes are placed above and below the cylinder. A 65×65 array of 90 nm apertures e-beam lithographed in 50 nm thick silicon nitride [22] is used as a weak link and is glued into the lower membrane. The use of two membranes permits independent measure and control of pressure differential, thus allowing feedback techniques to render ΔP constant over many seconds of measurement. Motion of the top diaphragm is sensed with a Paik-type displacement sensor [18]. The significant differences compared with the apparatus of Avenel and Varoquaux are (1) the use of an $N \times N$ array of nominally square nanoscale apertures instead of a single slit-like aperture and (2) the absence of an additional large channel shunting the weak link. Now the flow is associated only with the weak link leading to a direct interpretation of the weak-link properties.

A step voltage is applied between the top diaphragm and its adjacent electrode, thereby pulling up on the membrane. This creates a pressure difference ΔP across the weak link. If the aperture array is characterized by $I \propto \sin \phi$, the application of this chemical potential difference should cause the fluid to oscillate across the aperture array. Since the applied pressure is typically in the mPa range, as suggested in (15), the oscillation should be in the audible range. These Josephson oscillations are indeed observed [16].
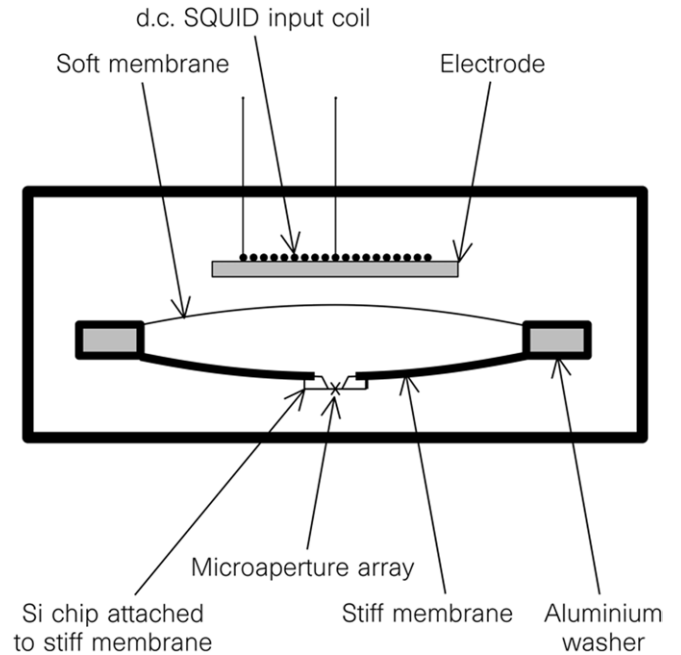
Due to dissipation [23] the pressure head decays over time and the output of the displacement sensor displays an oscillation signal in the audio range, sweeping downward in frequency. From such a transient, when the signal in a small time interval is Fourier transformed, it displays a clear peak. In each time interval, the average displacement of the diaphragm from equilibrium yields the pressure head ΔP. Figure 6 shows the frequency of the oscillation as a function of pressure across the weak link. A fit gives $194 \pm 15 \, \mathrm{Hz \, mPa^{-1}}$, verifying the Josephson frequency relation within the systematic error of the pressure gauge calibration.

Many ^{3}He weak-link experiments followed this direct observation of Josephson oscillations revealing fascinating similarities and dissimilarities with superconducting Josephson systems. The ^{3}He research culminated in the demonstration of a superfluid analog of a dc-SQUID. This superfluid ^{3}He quantum interference device (SHeQUID) exhibits a predicted modulation of the amplitude of the quantum oscillation when the device is reoriented with respect to the Earth's rotation axis (discussed in section 5.1). Although enlarging the pickup loop dimensions could yield a device useful for sensitive rotation measurements, the sub-mK technology associated with superfluid ^{3}He makes it an unlikely candidate for practical use. A review of the ^{3}He experiments is provided in [19].

3.5. ^{4}He Josephson oscillation

In 2001, hydrodynamic signatures consistent with $\sin \phi$ current–phase relation in superfluid ^{4}He were reported by Sukhatme *et al* [14]. The experimental apparatus contains a shunted weak link similar to the experiment of Avenel and Varoquaux depicted in figure 3. A single row of 24 slit-like apertures (170 nm by 3 μm in size separated by 10 μm)
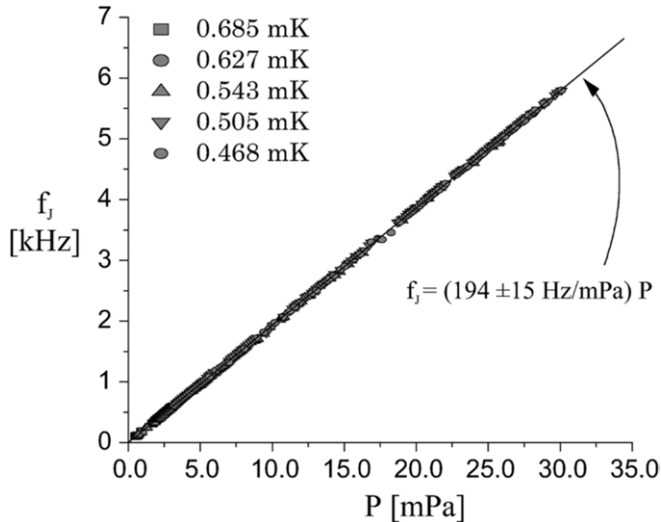
Figure 6. Frequency of Josephson oscillations versus the applied pressure difference for a ^{3}He weak-link array. Reprinted by permission from Macmillan Publishers Ltd: *Nature* [16], copyright 1997.

fabricated in a 150 nm thick membrane is used as the weak-link element and is shunted by a larger flow path. A diaphragm is coupled to form a hydrodynamic resonator, and a SQUID-based displacement sensor of sensitivity 2×10^{-13} m Hz$^{-1/2}$ is used to monitor the motion of the diaphragm. The resonator is driven at resonance and variations of the resonant frequency (due to the nonlinear inductance of the weak-link) are recorded as the drive level is changed. The experiment is carried out at temperatures 80 mK $> T_\lambda - T > 20\,\mu$K to take advantage of the diverging healing length near T_λ. The observed nonlinear response is consistent with a current–phase characteristic showing a sinusoidal form very close to T_λ, indicative of a weakly coupled Josephson regime. Staircase patterns observed in the amplitude versus drive data and the best fit model for the current–phase characteristics are shown in [14].

The discovery of Josephson oscillations in superfluid ^{4}He was reported by Hoskinson *et al* in 2005 [15]. The apparatus operationally is similar to that used in the Berkeley ^{3}He experiments and is sketched in figure 7. A cylindrical inner reservoir (diameter 8 mm, height 0.6 mm) is bounded on the top by a thin flexible diaphragm coated with a superconducting film. A 65×65 array of 70 nm apertures spaced $3\,\mu$m apart from each other is mounted in a rigid plate forming the walls and bottom of the inner reservoir. A SQUID-based displacement sensor with a sensitivity of 2×10^{-15} m Hz$^{-1/2}$ is used to track the diaphragm motion. As in the ^{3}He experiment of [16], a single flow path through a weak-link element is used without any parallel channel. The experiment is carried out in the temperature range of 2.9 mK $> T_\lambda - T > 1.7$ mK. A pressure difference (and hence the chemical potential difference) is established across the aperture array by the application of voltage step on the diaphragm, and Josephson oscillations are directly observed.

For superfluid ^{4}He, the temperature term in the chemical potential difference (14) is often just as important as the pressure term and cannot be neglected (as was the case in the ^{3}He work) in testing the Josephson frequency formula. In the
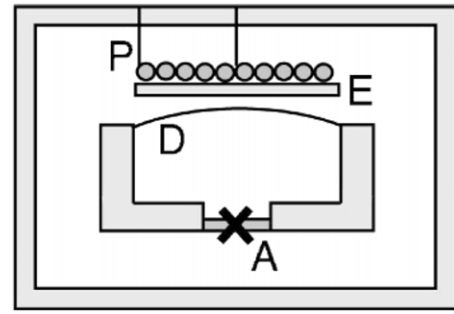

Figure 7. Experimental apparatus used for ^{4}He Josephson work at Berkeley. E: fixed electrode. D: soft diaphragm. A: aperture array. P: a SQUID-based transducer which monitors the position of the diaphragm.
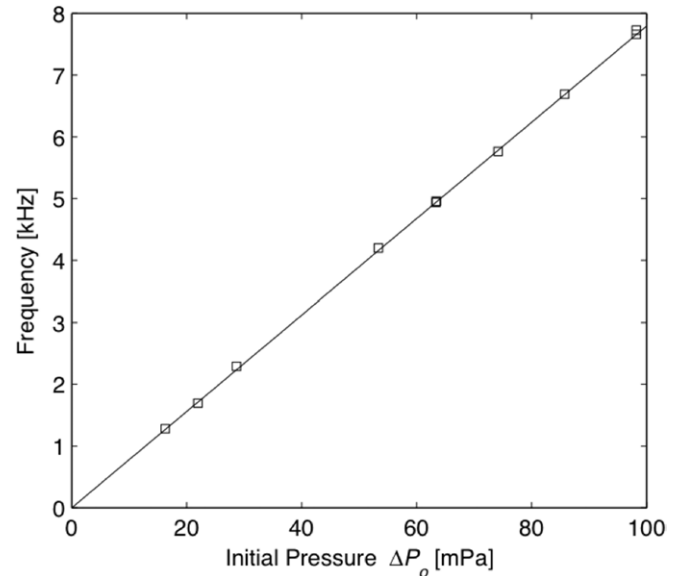

Figure 8. Frequency of ^{4}He Josephson oscillation versus initial pressure difference. Reprinted by permission from Macmillan Publishers Ltd: *Nature* [15], copyright 2005.

experiments of [15], there was no mechanism to determine the temperature difference between the inside and outside of the apparatus. However, at the initial instant ($t = 0$) of the pull on the diaphragm, the temperatures on both sides of the aperture array are equal, and the entire $\Delta\mu$ is determined by the initial pressure head ΔP_0. Therefore at $t = 0$, the Josephson frequency should be given by

$$f_J = \frac{\Delta\mu}{h} = \frac{m_4}{\rho h}\Delta P_0. \qquad (16)$$

In figure 8, the measured frequency of the observed oscillation is plotted against the initial pressure difference ΔP_0. A fit to the data gives a slope of 78 Hz mPa^{-1} with a systematic uncertainty of 20% arising from the pressure calibration. This agrees with (16), which predicts the value 68.7 Hz mPa^{-1}.

Both the ^{4}He experiment described above and the ^{3}He work of [16] demonstrate the Josephson frequency relation when the oscillations are driven solely by pressure differentials. To test the more general form of frequency relation with both ΔP and ΔT terms, Penanen and Chui suggested thermally driving Josephson oscillations [24]. This was accomplished by Hoskinson and Packard in superfluid ^{4}He [25]. The

experimental apparatus used is similar to that shown in figure 7 but with a heater installed in the inner reservoir.

When the heat is applied, the temperature differential ΔT between the inner cell and the outside bath is determined by the balance of four heat flows in the cell. The power applied to the heater W_h causes the inner temperature to increase. Normal current flowing out of the inner cell, $-I_n$, causes the inner temperature to decrease. Superfluid current I_s flowing into the inner cell causes cooling. Finally, thermal conduction through the walls of the inner cell acts to reduce ΔT. It can be shown [25] that ΔT evolves according to

$$C_p \frac{d\Delta T}{dt} = -sT\left(I_s - \frac{\rho_s}{\rho_n}I_n\right) - \frac{\Delta T}{R} + W_h, \qquad (17)$$

where ρ_s and ρ_n are the superfluid and normal fluid densities, R is the thermal resistance between the ^{4}He inside the inner cell and the ^{4}He outside, and C_p is the heat capacity of helium in the inner reservoir.

The normal fluid flow through the apertures obeys a Navier–Stokes equation with the addition of a ∇T term [3]. Flow through a constriction takes the form

$$I_n = -\frac{\rho_n \beta}{\eta}\left(\rho_n \frac{\Delta P}{\rho} + \rho_s s \Delta T\right), \qquad (18)$$

where β is a geometrical factor that can be determined [26] from normal flow measurements above T_λ, and η is the fluid viscosity. With this, (17) is numerically integrated to determine ΔT throughout the thermally driven Josephson oscillations. Figure 9 shows the time evolution of $m_4 \Delta P/\rho$ and $m_4 s \Delta T$ as well as the complete chemical potential difference as a function of time after a step heat is applied at $t = 0$. One can see that the equilibrium state of zero chemical potential difference is attained after the increases in temperature and pressure differentials. Hoskinson and Packard divided the transient into a sequence of small time intervals and determined the oscillation frequency in each interval using Fourier transforms. The frequency of oscillation as a function of $\Delta \mu$ is shown in figure 10. All points lie on a single line whose inverse slope gives $1.02 \pm 0.02h$, in excellent agreement with the general Josephson frequency formula $f_J = \Delta \mu / h$.

4. Strongly coupled quantum fluids

In the previous section, we have discussed the physics of two weakly coupled quantum fluids. As mentioned in section 3.2, the degree of coupling is determined by the ratio of aperture dimensions to the superfluid healing length. In this section, we discuss the case of strong coupling where the healing length is small compared with the apertures used to link two superfluid reservoirs. Surprisingly, even in this limit a type of oscillation occurs at the Josephson frequency.

4.1. Critical velocity and vortex dynamics

A superfluid is associated with a coherent ground state described by a wavefunction $\Psi \sim e^{i\phi}$. Applying the current operator $J = -(i\hbar/2m)(\Psi^*\nabla\Psi - \Psi\nabla\Psi^*)$ leads to (2): $v_s = (\hbar/m)\nabla\phi$. This is a fundamental equation connecting
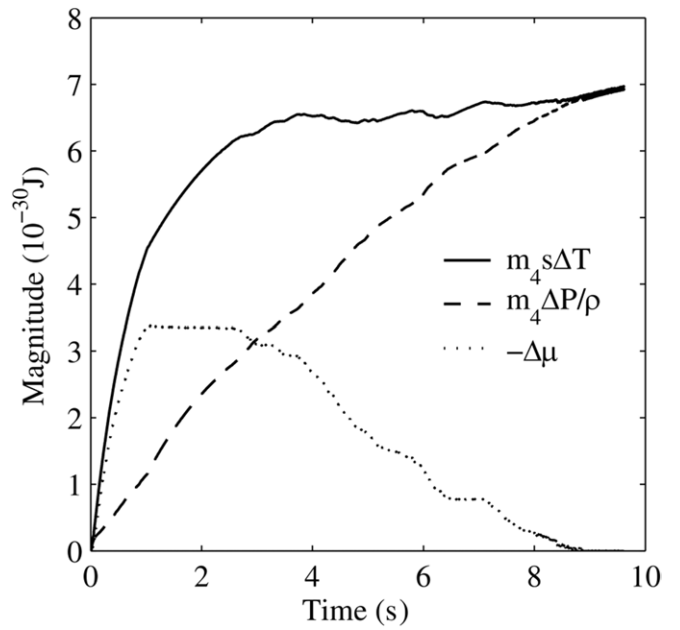

Figure 9. Evolution of $m_4 \Delta P/\rho$, $m_4 s \Delta T$ and $\Delta \mu$ as a function of time. The pressure $\Delta P(t)$ is directly measured while $\Delta T(T)$ is determined from the competing heat flows $T_\lambda - T = 1.5$ mK. Reprinted with permission from [25]. Copyright 2005 by the American Physical Society.
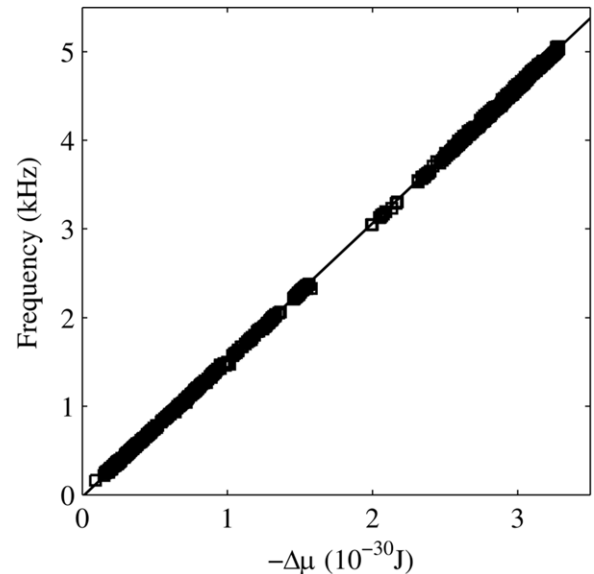

Figure 10. Frequency of Josephson oscillation versus the entire chemical potential difference (with both ΔP and ΔT terms). The gaps in frequency data correspond to intervals in which the oscillation amplitude has dropped below the background noise. Reprinted with permission from [25]. Copyright 2005 by the American Physical Society.

the two-fluid model of Landau with the macroscopic quantum picture introduced by London, Onsager and Feynman.

We consider again two baths of superfluid connected by a channel. If the channel is large compared with the healing length, the two baths are said to be strongly coupled and the Josephson current–phase relation does not hold. Rather, since $I \propto v_s \propto \nabla\phi \propto \Delta\phi$, the mass current is a linear function of phase difference. When a chemical potential difference is established between two baths, the phase difference across

the channel evolves at a rate proportional to the magnitude of the applied $\Delta\mu$ according to (10). The resultant gradient in phase is equivalent to the flow of superfluid through the aperture according to (2). A dc chemical potential difference then results in an accelerating unidirectional mass flow (unlike in the weakly coupled regime).

One of the defining properties of a superfluid is that it flows without dissipation up to some critical velocity. The Landau two-fluid model predicts an upper critical velocity of about $58\,\mathrm{m\,s^{-1}}$ after which elementary excitations can be copiously produced leading to dissipation. However, experiments show that for flow in narrow channels dissipation sets in at speeds about two orders of magnitude lower than the Landau limit. In these cases, dissipation takes place via the stochastic creation of quantized vortices, a characteristic superfluid flow phenomenon introduced by Onsagar [27] and Feynman [28].

If accelerated by a dc chemical potential difference, when the flow velocity at the channel's wall reaches a particular critical velocity, a quantized vortex is stochastically nucleated. This vortex moves across the channel, growing larger as time progresses, until it completely traverses the channel. Presumably, it finally encounters a boundary and is broken up into smaller and smaller segments, eventually becoming part of the background excitation bath, i.e. the normal fluid. Anderson [29] has shown that the vortex's traversal of the channel removes a fixed amount of energy from the channel flow and the phase difference across the channel drops by 2π. In this so-called 2π phase slip process, the flow velocity decreases by $\Delta v_s = \kappa/l_{\mathrm{eff}}$, where $\kappa = h/m^*$ is the quantum of circulation and l_{eff} is the effective hydrodynamic length of the aperture.

In superfluid ^{4}He, individual phase slip events were first observed by Avenel and Varoquaux [17] using the apparatus shown in figure 3. The resonator system is driven on resonance with an ac drive synchronized to the displacement sensor output. This results in the oscillation amplitude growing in time. When the velocity in the orifice reaches a critical velocity, a dissipative phase slip event takes place, resulting in the diaphragm's oscillation amplitude abruptly dropping. After such an event, the fluid is driven again over many cycles of oscillation until the velocity again reaches the critical velocity to repeat the same process. The peak amplitude of the diaphragm oscillation as a function of time is shown in figure 11. Individual phase slip events are apparent in the figure. The temperature dependence of the critical velocity [30–33] is consistent with a stochastic nucleation mechanism where an energy barrier for vortex creation is overcome by thermal fluctuation with a nucleation rate given by an Arrhenius law [34]. Relevant energy barriers and statistical variations in the critical velocity have been measured [35, 36] and explained phenomenologically [37, 38] although the nature of phase slip dynamics very close to T_λ is less well known.

Although in superfluid ^{4}He experiments reveal the onset of dissipation (due to vortex nucleation) at velocities much less than the Landau critical velocities, that is not the case with superfluid ^{3}He–B phase. There the first excitations are often quasiparticles produced by pair-breaking near $3\,\mathrm{cm\,s^{-1}}$ (at zero ambient pressure). Therefore the physics of phase slip
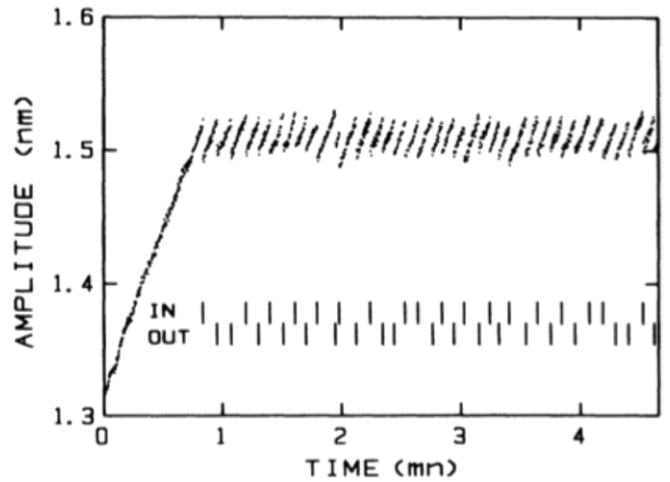

Figure 11. Peak amplitude of diaphragm oscillation versus time. Abrupt drops in the membrane oscillation amplitude mark individual phase slip events. Reprinted with permission from [17]. Copyright 1985 by the American Physical Society.

oscillations to be discussed in the next section applies only to superfluid ^{4}He.

We also note that superflow and critical behavior in ^{3}He–A phase are rather complicated due to textual effects at low velocities. These topics are beyond the scope of this review. Interested readers should refer to [11] and references within.

4.2. Phase slip oscillation

In the experiments of Avenel and Varoquaux that revealed individual phase slips, a double-path hydrodynamic resonator was driven with a sinusoidal drive at resonance. It is also possible to observe such phase slip events using the apparatus shown in figure 7 and by applying a dc chemical potential step across the aperture(s). The time derivative of (2) combined with (10) shows that the fluid acceleration is proportional to the applied chemical potential difference. Therefore, if one applies a constant chemical potential difference across an aperture, the fluid velocity increases linearly in time until it reaches the critical velocity v_c, at which point it abruptly decreases by an amount Δv_s. It is then followed by a linear increase in velocity and the process is repeated. The velocity profile of the superfluid flow through an aperture then resembles an asymmetric sawtooth. If there are no fluctuations in v_c, the abrupt phase slip events should take place with a regular time interval

$$\Delta t_{\mathrm{slip}} = \frac{\Delta v_s}{\dot{v}_s} = \frac{\kappa}{l_{\mathrm{eff}}}\left(\frac{\hbar}{m_4}\nabla\dot{\phi}\right)^{-1} = \frac{h}{\Delta\mu}. \tag{19}$$

The frequency of such phase slip events is then

$$f = \frac{1}{\Delta t_{\mathrm{slip}}} = \frac{\Delta\mu}{h}, \tag{20}$$

which happens to be identical to the Josephson frequency relation discussed in relation to the weakly coupled regime. This is not a coincidence since the phase-evolution equation (10) implies, for periodic phase changes of 2π, the frequency

8

of those changes must be simply $\Delta\mu/h$. In apertures smaller than $\sim 1\,\mu$m, simple 2π phase slippages are the characteristic dissipation events.

The temperature dependent phase slip critical velocity decreases towards zero as the temperature is increased toward T_λ. However, the velocity drop Δv_s is independent of temperature. Therefore when $v_c < \Delta v_s$, the flow actually reverses direction whenever a phase slip occurs. When v_c drops to $\sim\Delta v_s/2$, the phase slip oscillation would resemble a sawtooth of amplitude $\Delta v_s/2$ centered on $\langle v_s\rangle = 0$. This is the temperature regime where the the healing length becomes comparable to the aperture dimensions and the current–phase relation should become sine-like. The Josephson critical current (per aperture) I_c then must be on the order of $\rho_s\sigma_a\Delta v_s/2$ where σ_a is the effective cross-sectional area of the aperture and ρ_s is the suppressed superfluid density within the aperture.

The fact that the oscillations in both the weak-link case as well as that of strong coupling occur at the same frequency, $\Delta\mu/h$, implies a smooth morphing of one phenomenon to the other. These two distinct regimes as well the intermediate cross-over regime have been investigated in superfluid ^{4}He and are discussed further in appendix A. The significant point here is that in both regimes one can operate superfluid interferometers.

5. Quantum interference devices: proof-of-principle experiments

5.1. The SHeQUID as a Sagnac interferometer

One of the potentially practical applications for a superfluid quantum interference device is rotation sensing through the Sagnac effect [39]. When a SHeQUID such as that depicted in figure 1 is placed in a rotating frame, the superfluid is forced into quasi-solid body motion in a direction normal to the partition walls containing the weak links. If the interferometer is rotating with angular velocity $\vec{\Omega}$, the fluid in the connecting tubes moves with it and gives rise to a phase difference $\Delta\phi_{\text{ext}} = 4\pi\vec{\Omega}\cdot\vec{A}/\kappa$. Here $\vec{A}$ is the loop area vector. One can view this as the superfluid version of the optical Sagnac phase shift $\Delta\phi = 2\vec{A}\cdot\vec{\Omega}\omega/c^2$, where now the effective photon mass $\hbar\omega/c^2$ is replaced by the mass of the superfluid atom.

It follows from (4) that the overall oscillation amplitude from two junctions should modulate as a function of $\Delta\phi_{\text{ext}} \propto \vec{\Omega}\cdot\vec{A}$, making the device a rotation sensor. The potential sensitivity of this device compared with optical Sagnac interferometers stems from the fact that $\hbar\omega/c^2$ for visible photons is 10 orders of magnitude smaller than the helium atomic mass. This is the basic advantage of matter wave interferometers compared with optical devices. We note that the Sagnac phenomenon has been studied extensively in beams of light [40], neutrons [41] and atoms [42–44]. Some fundamental and practical differences and relative merits between various rotation sensors are briefly discussed in appendix F and G.

The first superfluid helium equivalent of a dc-SQUID, a device we refer to as a SHeQUID, was constructed using superfluid ^{3}He [45]. Its operation was demonstrated with
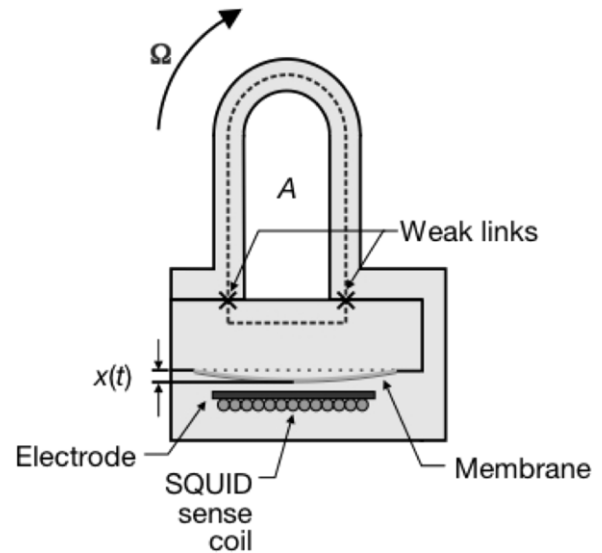

Figure 12. Schematic of ^{3}He interferometer. The shaded regions are filled with superfluid ^{3}He. The closed path through two weak links (indicated by the dotted line) defines the instrument's sensing area A. The diaphragm position is detected with a SQUID-based displacement transducer. Reprinted by permission from Macmillan Publishers Ltd: *Nature* [45], copyright 2001.

interference through the Sagnac effect induced by the Earth's rotation. The apparatus schematic is shown in figure 12. A superfluid torus is interrupted by two weak links (each one with 65×65 array of nominally 100 nm apertures etched in a 60 nm thick silicon nitride membrane) with a diaphragm, electrode, and a displacement sensor placed near the junctions as in the case of a single weak-link experiment. The area vector of the loop points horizontally in the laboratory which is located at approximately $38°$N. Since the Earth is spinning with an angular vector pointing north, the rotation 'flux' $(\vec{\Omega}\cdot\vec{A})$ in the loop can be varied by reorienting the interferometer about the vertical axis in the lab frame.

This reorientation method has also been used in superfluid ^{4}He to show that rotation flux could vary the phase slip critical velocity in an aperture [46, 47], and in superfluid ^{3}He to change the frequency in a nonlinear Helmholtz oscillator containing a single Josephson weak link [48]. These devices use only one weak link rather than two and resemble rf-SQUIDs. They have been called phase slip gyroscopes or gyrometers and are briefly discussed in appendix F.

For the apparatus shown in figure 12, the sensing area $A \sim 6\,\text{cm}^2$ is chosen so that the rotation of the Earth, Ω_E, can induce more than one cycle of the modulation pattern while reorienting the cryostat $180°$ in the lab frame. The mass current oscillation amplitude is measured with the same Fourier transform techniques used for the single weak-link experiments and is plotted as a function of $\vec{\Omega}\cdot\vec{A}$ in figure 13. The result shows a classic double-path interference pattern, making this the first direct analog of a dc-SQUID in a superfluid system. This experiment, which employed superfluid ^{3}He–B, was carried out below 1 mK using nuclear adiabatic demagnetization cryogenics.

Soon after the discovery of Josephson oscillations in superfluid ^{4}He, a ^{4}He quantum interference device was
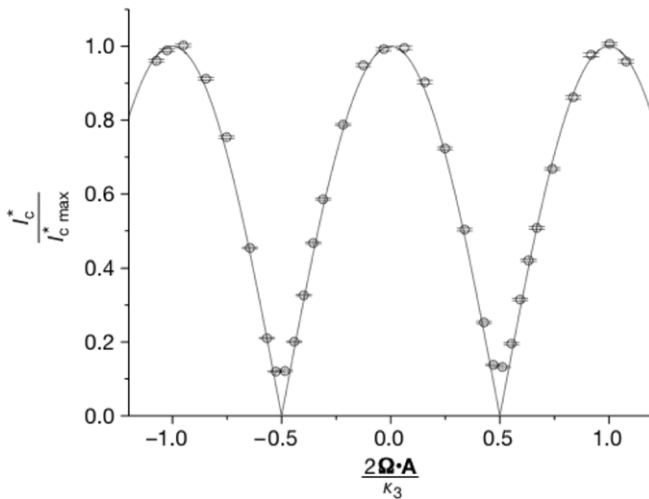
Figure 13. ^{3}He mass-current oscillation amplitude versus rotation flux $\vec{\Omega} \cdot \vec{A}$. Reprinted by permission from Macmillan Publishers Ltd: *Nature* [45], copyright 2001.

constructed [49]. The apparatus used for proof-of-principle rotation sensing is depicted in figure 14. The device with a sensing area of $\sim$10 cm^2 operates on the same Sagnac principle as the ^{3}He gyroscope discussed above but at a temperature two thousand times higher. Two 65×65 arrays of nominally 90 nm apertures are placed in a loop of superfluid ^{4}He. The interference pattern as a function of rotation flux is shown in figure 15. Larger amplitude modulation patterns are obtained in a strongly coupled phase slip regime while smaller ones are taken closer to T_λ (deeper in the Josephson regime). The fact that the interference pattern persists when the current–phase relation is no longer sinusoidal shows the robust nature of this phenomenon.

The sensitivity of this type of device can be estimated by multiplying the steepest inverse slope of figure 15 by the smallest detectable current $\delta I = \rho a \omega \delta x$, where $a = 0.5$ cm^2 is the diaphragm area, ω is the Josephson frequency, and $\delta x \sim 3 \times 10^{-15}$ m is the smallest displacement that can be detected in a 1 Hz bandwidth (limited by electronic noise in the displacement sensor circuit). The intrinsic phase sensitivity of the first prototype device is $\sim 3 \times 10^{-2}$ rad Hz$^{-1/2}$, which corresponds to angular velocity resolution of $\sim 2 \times 10^{-7}$ rad s^{-1} Hz$^{-1/2}$.

The device sensitivity improves with several variables including the enclosed sensing area, the number of apertures in the junction, the number of turns in the sensing loop and the operating frequency. It is also possible to make a grating structure rather than a double-path configuration and also to amplify the interference signal using nonlinear dynamics. We describe some of these techniques in section 6. Although analysis of the thermal noise limits of related devices has been performed [50], the corresponding limit for this neutral matter interferometer is not yet known. Phase fluctuations ($\sim N^{-1/2}$ where $N \sim 10^{21}$ is the number of atoms in the device) may be the ultimate noise source but a practical limitation is normally the vibration and rotation coupling from the environment. Successful development of this interferometer to detect minute phase changes (i.e. small rotation rates) would require a rigid
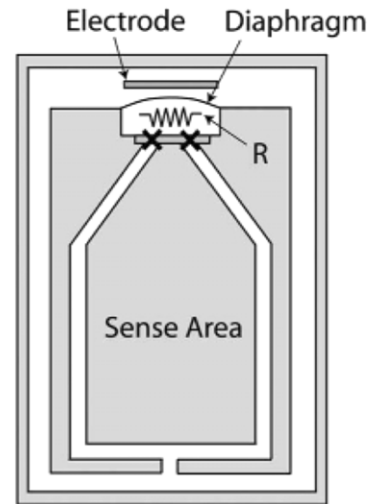

Figure 14. Schematic of ^{4}He interferometer. The Xs indicate the positions of the two aperture arrays. The unshaded regions are filled with superfluid ^{4}He. Pressure differential across the aperture arrays is created by application of an electrostatic force between the diaphragm and electrode. The resistor R is a heater which can contribute to the chemical potential difference. The interferometer sits inside a can (outer shaded border), and the can is immersed in a temperature regulated ^{4}He bath. Reprinted with permission from [49]. Copyright 2006 by the American Physical Society.
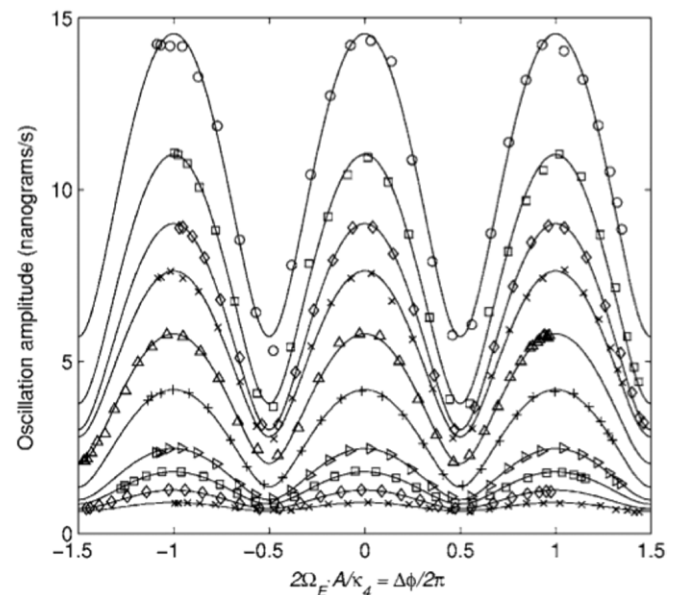

Figure 15. ^{4}He mass-current oscillation amplitude versus rotation flux $\vec{\Omega} \cdot \vec{A}$. The modulation height increases with lowering of the temperature. From top to bottom, the modulation curves are taken at temperatures $T_\lambda - T = 12, 7, 4, 3, 2, 1.5, 0.9, 0.6, 0.4,$ and 0.3 mK. Reprinted with permission from [49]. Copyright 2006 by the American Physical Society.

structure placed in a quiet environment as is done with large laser interferometers [51].

5.2. The SHeQUID as a phase gradient meter

Because of its sensitivity to externally induced quantum phase gradients, a superfluid quantum interference device can
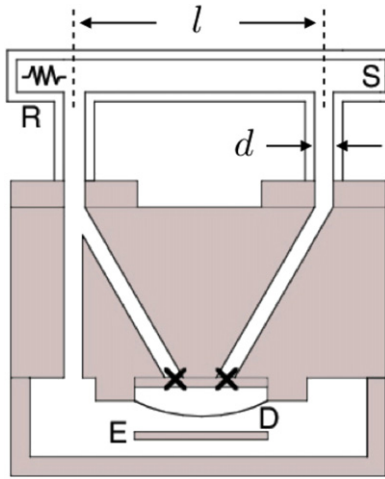
Figure 16. Apparatus for measuring phase gradients driven by a heat current. Flexible diaphragm (D) and electrode (E) form an electrostatic pressure pump. A resistive heater (R) and a thin Cu sheet (S) serve as a heat source and a temperature sink, respectively. Crosses indicate the aperture arrays. Each array consists of 100×100 30 nm apertures spaced on a 3 μm square lattice in a 60 nm thick silicon nitride window. Reprinted with permission from [53]. Copyright 2007 by the American Physical Society.

be employed to probe aspects of fundamental physics that have remained elusive in the past. One such example is an experiment that investigated the connection between the wavefunction picture [52] of superfluid helium and Landau's two-fluid model [4]. As mentioned in section 4.1, applying a current density operator to a wavefunction $\Psi \sim e^{i\phi}$ yields the relation (2): $v_s = (\hbar/m)\nabla\phi$, where this velocity is interpreted as that of the superfluid component in the framework of Landau's two-fluid model. This relation has been used to understand various physical phenomena such as the existence of vortices and quantized circulation. However a direct verification of (2) has been elusive due to the lack of an appropriate phase-measuring device. This situation has changed with the invention of a ^{4}He SHeQUID.

The experimental apparatus is depicted in figure 16 [53]. The topmost tube (of length l and cross-sectional area σ) contains a resistive heater at one end and a thin copper sheet at the other. These serve as a heat source and a sink, respectively. When power $\dot{Q}$ is applied to the heater, the two-fluid model predicts that the normal component flows away from the heat source while the superfluid component flows toward it with velocity

$$|v_s| = \frac{\rho_n}{\rho \rho_s T s \sigma}\dot{Q}. \tag{21}$$

Here ρ and ρ_n are total and normal fluid densities, T is the temperature and s is the specific entropy [3]. Thus the power in the heater produces a uniform v_s, which should correspond to a constant phase gradient $\nabla\phi_{heat}$ along the top arm. The phase difference between the ends of the two vertical arms $\Delta\phi_{heat} = l\nabla\phi_{heat}$ can be monitored by configuring the top tube as part of a SHeQUID loop as shown in figure 16. If the wavefunction picture and the two-fluid model are consistent with each other, the interferometer output should modulate with oscillation
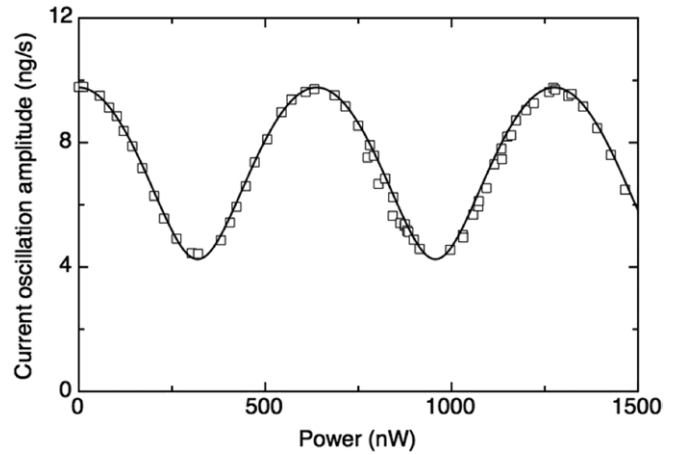

Figure 17. Mass-current oscillation amplitude versus power injected into the top tube [53]. These data are taken at $T_\lambda - T \approx 16$ mK. The cryostat is oriented to catch just the right amount of rotation flux from the Earth in the interferometer loop so that the mass-current oscillation amplitude is at maximum with zero power injected into the top tube. Reprinted with permission from [53]. Copyright 2007 by the American Physical Society.

amplitude $\propto \sqrt{\cos^2(\Delta\phi_{ext}/2) + \gamma^2 \sin^2(\Delta\phi_{ext}/2)}$, where

$$\Delta\phi_{ext} = \frac{m}{\hbar}\frac{l}{\sigma}\frac{\rho_n}{\rho \rho_s T s}\dot{Q}. \tag{22}$$

Figure 17 shows the measured interferometer output as a function of heat input in the top tube. The solid line is a fit using (22). The periodic variation in the output as a function of $\dot{Q}$ shows that there is indeed a uniform phase gradient across the topmost tube such that $\nabla\phi \propto v_s$. The distance between two adjacent maxima seen in figure 17 is the power that leads to a 2π phase change across the heat current tube. Figure 18 shows these powers ($\dot{Q}_{2\pi}$) measured at different temperatures. From the formulation above, one can write $\dot{Q}_{2\pi} = (h/m)\beta(T)$, where $\beta(T) \equiv (\sigma/l)(\rho\rho_s T s/\rho_n)$. The function $\beta(T)$ can be computed with published tabulation on ρ_s, ρ_n, ρ and s, and the designed values of l and σ. This function multiplied by a constant to fit the data is shown as the solid line in figure 18. The best multiplication factor is $(9.1 \pm 0.9) \times 10^{-8}$ m^2 s^{-1}, which agrees with the expected value of $h/m = 9.97 \times 10^{-8}$ m^2 s^{-1} within the systematic uncertainty involved in length l and the unknown velocity profile. This result directly demonstrates the fundamental relation linking the macroscopic wavefunction picture and the two-fluid description of superfluid helium while showing the novel nature of the superfluid interferometer as a quantum phase-measuring device.

5.3. Flux-locking with a heat tube: linearization of the SHeQUID

Interferometers typically have a transfer function wherein the output amplitude is a cosinusoidally varying function of some variable of interest. For example, in the case of a SHeQUID, the interference amplitude is given by $\propto F(\Delta\phi/2) \equiv [\cos^2(\Delta\phi/2) + \gamma^2 \sin^2(\Delta\phi/2)]^{1/2}$. This
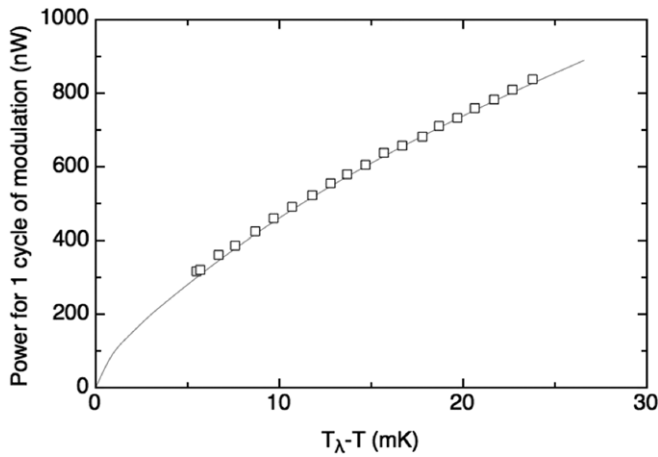
Figure 18. Power needed to cause the oscillation amplitude to move from one maximum to the next. Reprinted with permission from [53]. Copyright 2007 by the American Physical Society.

nonlinearity is problematic because the sensitivity of the device then varies with the signal of interest. To achieve practical utility, it is useful to have a method to linearize the instrument's response at the point of maximum sensitivity. The heat current technique that injects phase variations into a superfluid interferometer (discussed in the preceding section) can be used as a feedback element necessary for linearization.

A circuit equivalent to the apparatus shown in figure 16 is represented in figure 19. If $\Delta\phi_{\rm ext}$ is the phase shift due to some external influence and $\Delta\phi_{\rm heat}$ is the phase shift due to a heat current in the top arm, the overall oscillation amplitude should be modulated as $\propto F(\Delta\phi_{\rm ext}/2 + \Delta\phi_{\rm heat}/2)$ [54]. The key for linearization is to adjust $\Delta\phi_{\rm heat}$ to always nullify $\Delta\phi_{\rm ext}$. Figure 20 demonstrates this operation. As a proof-of-principle experiment, the Sagnac phase shift due to the Earth's rotation has been used as the external phase shift. As seen in section 5.2, $\Delta\phi_{\rm heat} \propto \dot{Q}$. The Sagnac signal $\Delta\phi_{\rm ext} \propto \vec{\Omega} \cdot \vec{A}$. Then the interference amplitude varies with $\propto F(a\vec{\Omega} \cdot \vec{A} + b\dot{Q})$, where $a \equiv 2\pi m/h$ and $b \equiv (l/\sigma)(\pi m/h)(\rho_n/\rho\rho_s Ts)$ are constants at given temperature. Figure 20(a) shows the signature sinusoidal interference pattern due to the reorientation of the device loop about the vertical with no feedback applied. Figure 20(b) shows the same measured amplitude, this time with power applied to the heater thereby creating a phase shift in the heater tube. The changes in rotation flux are cancelled by manually adjusting the appropriate heater power to keep the argument of F constant. The interferometer is thus maintained at fixed oscillation amplitude and the total loop phase shift is locked at the point of steepest slope in the interference curve. Within the noise level of the experiment, $a\vec{\Omega} \cdot \vec{A} + b\dot{Q} = {\rm constant}$. Figure 20(c) shows the heater power injected plotted against rotation flux. It is seen that $\dot{Q} \propto \vec{\Omega} \cdot \vec{A}$. Thus the amount of power needed for this purpose provides a linear measure of the change in rotation flux: $|\vec{\Omega} \cdot \vec{A}| = b\dot{Q}/a$.

In practice, this feedback scheme works for injected heater power values lower than that corresponding to 250 complete cycles in figure 20(a). For heater power values greater than this limit, a rapid onset of quantum turbulence is seen, rendering the interferometer useless for measuring external phase shifts.
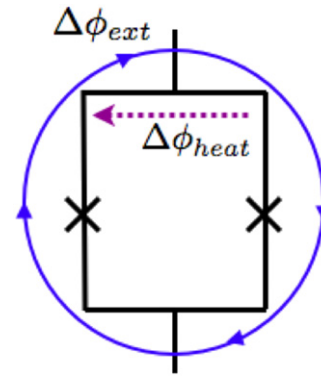

Figure 19. Equivalent SQUID circuit. $\Delta\phi_{\rm ext}$ is the phase shift produced by some (possibly globally acting) external influence, which the SHeQUID is being used to measure. $\Delta\phi_{\rm heat}$ is the phase shift due to injected heater power.
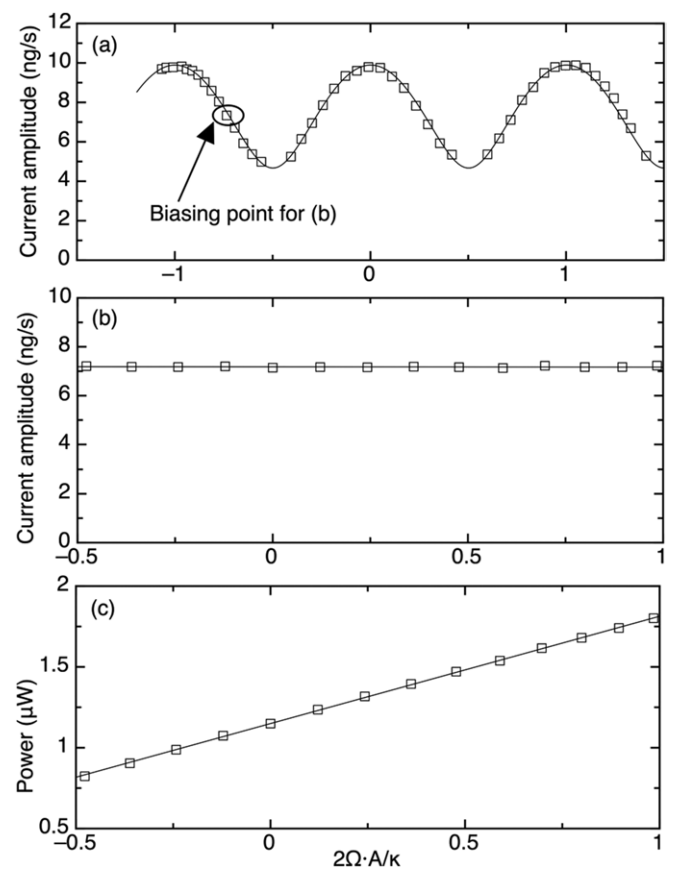

Figure 20. (a) Interferometer output modulation due to Sagnac effect. (b) Modulation compensated by injected heater current thus making the interferometer output independent of the rotation flux. (c) Feedback heater power needed for a given value of rotation flux to maintain the interferometer output constant. Reprinted with permission from [54]. Copyright 2007, American Institute of Physics.

Recently a technique called 'history tracing method' has been suggested by Zheng *et al* [55] to achieve wider dynamic range for practical rotation sensing with a SHeQUID. This technique has not yet been tested.

If the heat flow pipe is filled with a packed powder or other porous medium, the critical velocity for the onset of vortex

creation and motion may be raised, leading to a wider dynamic range of linearization. This pinning technique also has not yet been tested, and increase in flow impedance as well as fountain pressure effects need to be considered.

The flux-lock feedback technique described in this proof-of-principle experiment involves Fourier transforming the Josephson oscillation signal in real time to determine its amplitude and thus the location in the modulation curve. The response time for such operation is limited by the Josephson frequency. For example, if 20 cycles of a 5 kHz signal are used for Fourier transforms, each measurement takes 4 ms. The system will not be able to remain locked to external phase influences that change at much faster rates. Using the chemical potential battery technique described in section 6.1 may remove this limitation. At this time the limiting slew rate of a SHeQUID using this technique is not known.

5.4. Detection of quantized vortex motion: the onset of quantum turbulence

As mentioned in section 4.1, if a quantized vortex line passes across a channel containing axial superflow, the vortex could grow in size at the expense of the channel's flow energy. A vortex completely crossing the channel leads to a 2π decrease in the quantum mechanical phase difference between the two ends of the channel. In macroscopic tubes (i.e. dimensions transverse to flow greater than 1 μm), the onset of dissipation (i.e. vortex crossing) usually occurs abruptly due to an instability and growth of preexisting pinned vorticity [56, 57]. Although the growth of quantum turbulence and the associated dissipation in large channels has been studied for over five decades, there is not yet a complete picture that describes the initial instability and the subsequent dynamics of the quantum vortices [58]. Since the SHeQUID is sensitive to changes in quantum phase, it provides a new tool to investigate vortex motion in a macroscopic passage.

In an apparatus such as that depicted in figure 16, the interferometer monitors the phase difference $\Delta\phi$ across the topmost tube. If a vortex initially pinned at the wall moves transversely across the tube, $\Delta\phi$ will change by 2π. In operation, the interferometer output is given by (4). Therefore, as the power $\dot{Q}$ is increased, the phase difference $\Delta\phi$ increases proportionally, and the interferometer signal varies cosinusoidally with $\Delta\phi$. For a fixed power, $\Delta\phi$ is constant in time (see figure 21(a)). However at some critical power $\dot{Q}_c$, previously pinned vortices start to traverse the channel, causing $\Delta\phi$ to cycle from 0 to 2π and the interferometer signal oscillates in time. Such an oscillation caused by a series of smoothly evolving 2π phase slippages is shown in figure 21(b). In the operating temperature range of the SHeQUID used in this experiment [59], the values of v_c (obtained from (2) and the observed value of $\dot{Q}_c$) are temperature independent with a mean of 1 mm s^{-1} and a standard deviation of 0.2 mm s^{-1}.

The frequency of phase slippage as a function of axial superfluid velocity is shown in figure 22 for various temperatures. It is apparent that in addition to the sudden onset of the phase variation at a critical velocity v_c, there are transitions to different oscillation frequencies creating
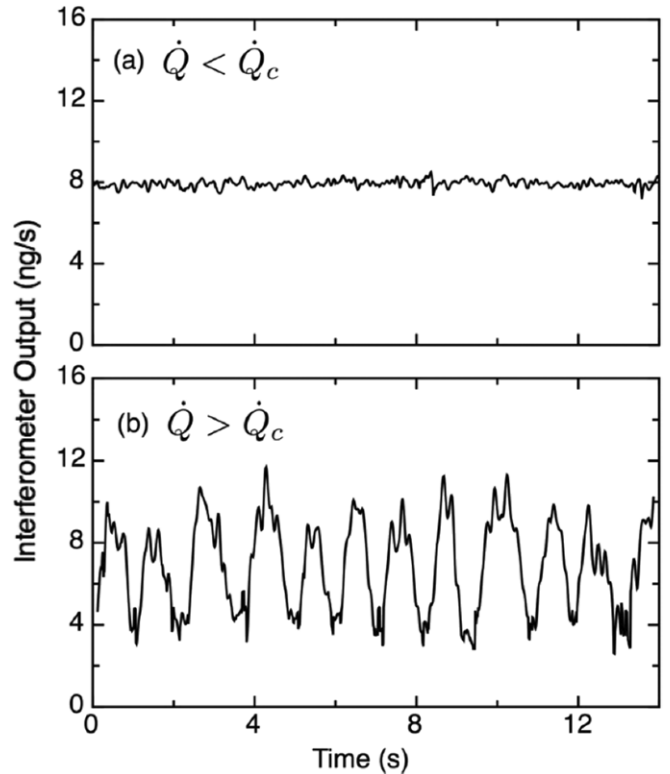

Figure 21. Interferometer output versus time. (*a*) $\dot{Q} < \dot{Q}_c$ and (*b*) $\dot{Q} > \dot{Q}_c$. These data are taken at $T_\lambda - T \approx 16$ mK. Note that the slow frequency of vortex crossing ($\sim$1 Hz) represents another example of the Josephson frequency relation. Reprinted with permission from [59]. Copyright 2007 by the American Physical Society.

plateaus. This unexpected discovery is just one more example of how a novel instrument uncovers new phenomena. There is as yet no explanation for this observation.

The investigation of ^{4}He properties in the presence of finite heat flux close to T_λ has drawn much interest [60, 61] since superfluid is considered to be a clean system suited for studying nonlinear critical phenomena. However, if the flow reaches the critical velocity for vortex crossing and dissipation sets in, the superfluid is no longer such an ideal testing ground. Traditionally the onset of extrinsic processes has been detected by a change in some macroscopic property such as the pressure head across the ends of the flow passage [62] or by attenuation of second sound [63] or propagating ion beams [64]. Since these techniques require a minimum amount of quantized turbulence to raise the signal of interest above the instrumental noise, they are not sufficiently sensitive to monitor the motion of a single vortex. The SHeQUID with its sensitivity to the motion of even a single vortex may be an ideal instrument to employ in these studies.

Recently, small hydrogen particles [65] and fluorescent techniques [66] have been used successfully as tracers in superfluid ^{4}He allowing the observation of vortex cores. Combined with such methods, a SHeQUID that allows the measurement of quantum phase changes may become a useful tool in studying the initial instability process of trapped vorticity and may yield further insights into the mechanisms that lead to the growth of quantum turbulence.
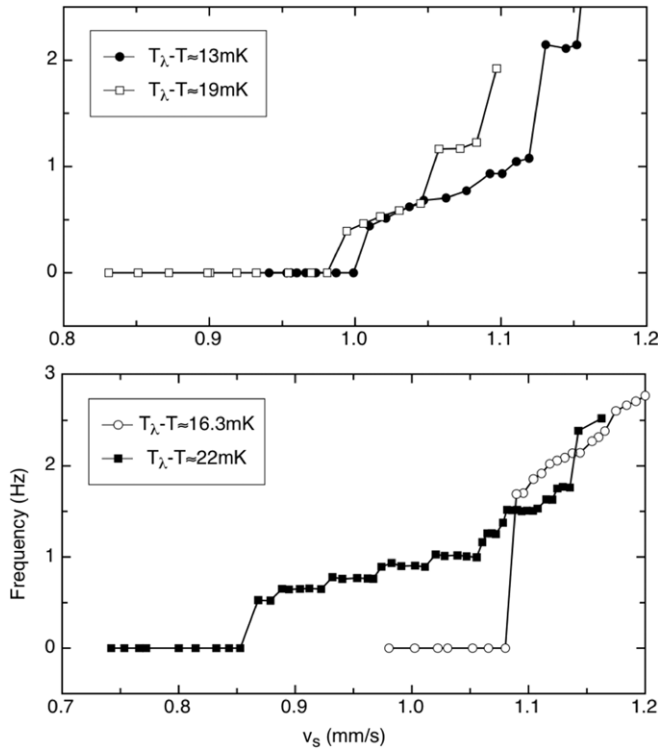
Figure 22. Vortex crossing frequency versus superfluid velocity in the channel. Zero frequency means that the interferometer signal is constant in time. Reprinted with permission from [59]. Copyright 2007 by the American Physical Society.

6. Techniques

6.1. Chemical potential 'battery'

In operating SHeQUIDs as described thus far, a flow transient is created by applying a static electrostatic force to a flexible diaphragm pump. With this method it is important to consider the measurement time required for particular applications. Superfluid ^{4}He quantum oscillations obey the Josephson frequency relation $f_J = \Delta\mu/h$, where $\Delta\mu = m(\Delta P/\rho - s\Delta T)$. These oscillations are accompanied by a finite dc fluid flow component driven by $\Delta\mu$. This dc flow causes the applied $\Delta\mu$ to decay over time, lowering the Josephson frequency and eventually ending the oscillations as $f_J \to 0$. Using feedback techniques [67], it is possible to hold the frequency constant for a short interval, but the measurement time is typically less than 30 s. This time limit is set by the limit of feedback voltage that can be applied to the diaphragm and also by the dynamic range of superconducting electronics utilized in the displacement transducer. This corresponds to, for example, a few 10 000 oscillation cycles for a ~1 kHz signal for one pull on the diaphragm (or a few thousand Fourier spectra to average over if transforms are taken from ~30 cycles of oscillation in time domain). This is sufficient for many experiments where one can induce a phase shift of interest and measure it at the same time. However, it is not ideal for applications where much longer measurement times are required or in cases where one needs to wait for a signal of interest to arrive (e.g. application in seismic studies). A technique we call a constant chemical

potential battery has been developed to maintain a fixed $\Delta\mu$ for indefinite times.

This technique was first demonstrated in a single array apparatus [68] and then applied to a double-path quantum interference device [69]. The interferometer configuration is similar to that shown in figure 16. When power is applied to a second heater placed in the small inner volume (between the junctions and the diaphragm), the superfluid fraction of the fluid flows toward that inner volume while the normal fraction flows out. The entropy is carried by the normal flow and thermal conduction through the wall. If the applied heat is small enough, after short transient behavior, a steady state is established such that $\Delta\mu = 0$. However, as the applied power is raised further, the superflow eventually reaches a critical velocity that limits the supercurrent. A new steady state is then established where $\Delta\mu$ is nonzero and constant, determined by the applied power. This constant $\Delta\mu$ drives Josephson oscillation continuously within the aperture arrays, and the oscillation frequency can be varied by adjusting the heater power. This technique allows truly continuous phase sensing mode of operation. It is essentially equivalent to using a battery to drive Josephson oscillation in superconducting weak-link systems. Due to nonlinearities in the weak-link flow properties there is a strong tendency for the chemical potential battery technique to force the quantum oscillations to occur at a cell resonance. Cell resonances excited by the quantum oscillations produce a homodyne mixing (see the following section) which creates additional dc currents thus keeping the "battery" potential constant for even lower heater powers. As yet the details of this mechanism is not well understood.

6.2. Fiske amplification

Since the mass-current oscillation is detected by a flexible diaphragm hydraulically coupled to the oscillating superfluid, the signal can interact with acoustic resonances within the apparatus, leading to substantial amplification with remarkable stability at particular frequencies. This is related to the superconducting Fiske effect [70], where the interaction of the Josephson oscillation with internal electrodynamic resonances in the junctions causes dc currents. This nonlinear phenomenon has been investigated in more detail in a single weak-link ^{3}He system in the context of resonant dc current enhancement [71] (see figure 23 for example), but its application as an amplifier has only been demonstrated for a ^{4}He quantum interference device.

The diaphragm velocity oscillation amplitude as a function of $\Delta\phi_{ext}$ for a ^{4}He interferometer is shown and marked as curve (a) in figure 24 [69]. For this curve, using the constant $\Delta\mu$ method, Josephson oscillations are driven in a spectral region where no resonant features exist. The modulation amplitude (i.e. difference between maxima and minima) seen in these particular data is representative of those observed in other experiments discussed in section 5. This curve should now be compared with curve (b) taken on resonance. A significant signal amplification is clearly visible. The sensitivity enhancement is ~34 comparing these two curves. We emphasize that, to harness this type of resonant
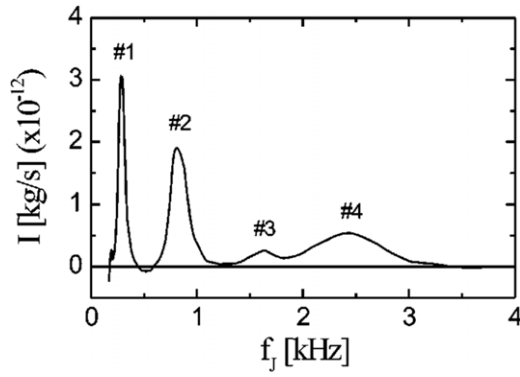
Figure 23. Amplitude of ^{3}He Josephson oscillation versus the oscillation frequency. Significant enhancement in mass current can be seen at several distinct resonant mechanical modes. Reprinted with permission from [71]. Copyright 1998 by the American Physical Society.
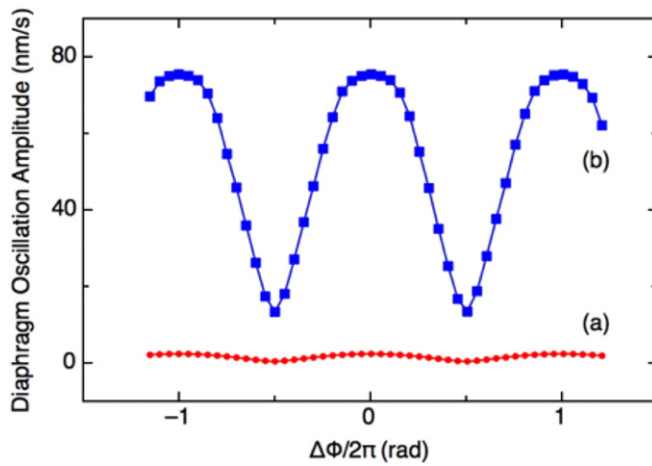

Figure 24. (*a*) ^{4}He interferometer output versus $\Delta\phi$. (*b*) The same pattern probed on resonance with Fiske amplification. Reprinted with permission from [69]. Copyright 2010 by the American Physical Society.

amplification, sufficient vibration isolation is necessary. Any excess environmental noise kicks up the resonances rendering the reliable observation of Josephson amplitude modulation difficult at those exact frequencies.

The Fiske amplification tends to make the chemical potential battery technique unusable at arbitrary frequency. If the oscillation frequency driven by the heater is near a cell resonance, the Fiske dc current increases the current in the apertures and pulls $\Delta\mu$ to that value that would continue to excite the resonance. This enhances the frequency stability of the interferometer. In the future, investigation with ac pressure and thermal drives in conjunction with modeling and simulation may allow one to engineer a particular resonance into an apparatus to further enhance the sensitivity.

The intrinsic phase sensitivity for the device demonstrated here with Fiske amplification is measured to be 8×10^{-4} rad Hz$^{-1/2}$. This is equivalent to a circulation change of $\sim 10^{-4}\kappa_4$, comparable to the fractional magnetic flux changes seen in the early development of dc-SQUIDs. Used as a gyroscope (with ≈ 10 cm^2 enclosed area), this translates to a rotational resolution of 8×10^{-9} rad s^{-1} Hz$^{-1/2}$,
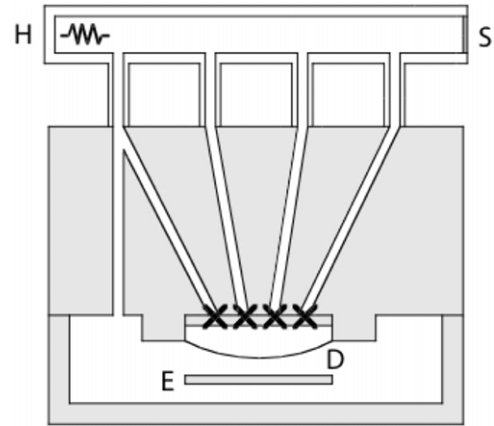

Figure 25. Interferometer with four junctions. The Xs indicate the weak-link junctions. D: soft diaphragm. E: fixed electrode. H: heat source. S: heat sink. Reprinted with permission from [78]. Copyright 2008 by the American Physical Society.

which surpasses typical sensitivities of conventional atom interferometers [72–74] and comes within an order of magnitude to the short-term sensitivity of the best reported dual atom interferometer (6×10^{-10} rad s^{-1} Hz$^{-1/2}$ [42]).

6.3. A superfluid interference grating

Since superfluid interferometry relies on measuring the change in quantum oscillation amplitude as a function of external phase shift, the sensitivity of the device is proportional to the slope of the interference pattern at its steepest point. This sensitivity can be increased by placing more than two arrays in parallel thus narrowing the peaks in the interference pattern. In the context of superconducting devices, Feynman suggested the importance of such a device as a magnetometer (often called a superconducting quantum interference grating (SQUIG)) [5]. This technique was first demonstrated experimentally with six point contacts in 1966 [75]. A similar configuration can in principle be employed in a superfluid system.

The device shown in figure 25 consists of four weak-link junctions placed in parallel in a loop filled with superfluid ^{4}He. Each weak link is a 50×50 array of nominally 90 nm diameter apertures (spaced 3 μm apart) etched in a 60 nm thick silicon nitride membrane. The topmost tube contains a heat source and sink, which are used to inject external phase shift by means of a heat current as described in section 5.2. If N identical weak links (each with current amplitude I_0) are used in the grating, the system should behave like a single junction with effective amplitude that modulates as [76, 77]

$$I_0 \left| \frac{\sin(N\Delta\phi/2)}{\sin(\Delta\phi/2)} \right|. \tag{23}$$

Numerical analysis of this equation shows that the slope at the steepest part of the interference pattern ($|\mathrm{d}I/\mathrm{d}\Delta\phi|_{(\text{max})}$) increases as [77]

$$\frac{|\mathrm{d}I/\mathrm{d}\Delta\phi|_{\text{grating(max)}}}{|\mathrm{d}I/\mathrm{d}\Delta\phi|_{\text{2-path(max)}}} \approx 0.2N^2, \tag{24}$$
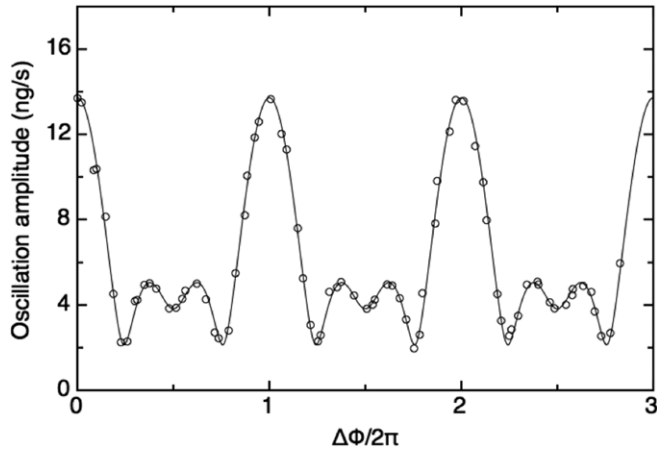
Figure 26. Mass-current oscillation amplitude versus $\Delta\phi$. The solid line is a fit where $I_2 = 0.90I_1$, $I_3 = 1.41I_1$ and $I_4 = 0.46I_1$. These data are obtained at $T_\lambda - T \approx 4$ mK. Reprinted with permission from [78]. Copyright 2008 by the American Physical Society.

Figure 27. Apparatus used to demonstrate interference from a single junction. A: aperture array. E: fixed electrode. R: heat source used to create phase gradient. P: SQUID-based transducer which monitors the position of the diaphragm (D). Reprinted with permission from [80]. Copyright 2011 by the American Physical Society.

where $|\mathrm{d}I/\mathrm{d}\Delta\phi|_{\text{2-path(max)}}$ is the maximum slope of the double-path interferometer. This implies, for example, that a grating structure with 10 weak links should give a phase change sensitivity $\sim$20 times greater than that of a double-path interferometer. If the weak links used are not identical with different oscillation amplitudes I_0, I_1, $I_2 \ldots$, I_{N-1}, the total mass-current oscillation amplitude can be written as $[A[0] + 2\sum_{k=1}^{N-1} A[k]\cos(k\Delta\phi)]^{1/2}$, where $A[k] \equiv \sum_{q=0}^{N-1-k} I_q I_{q+k}$.

In addition to the N^2 sensitivity enhancement there is another more subtle advantage to using a grating structure. This involves the effect of the inevitable variations among weak-link junctions used in the interferometer. Because of the limitations of nanofabrication, all the junctions cannot be made identical. However, in a grating configuration the modulation depth is affected less by nonuniformities compared with a conventional double-path setup. For example, in the extreme case where one of the junctions has zero oscillation amplitude, a grating structure will still exhibit deep modulation and can be used as a sensitive interferometer. In contrast, a double-path interferometer would show no modulation, giving zero sensitivity.

Figure 26 is an example of experimental data showing mass-current oscillation amplitude as a function of $\Delta\phi$ for a four-path SHeQUID [78]. A striking similarity to four-slit optical interference pattern can be seen. The slope at the steepest part of the interference pattern for this grating is found to be $\sim$4.3 times larger than that of a previous superfluid ^{4}He double-path interferometer operating at the same temperature.

In the case of a SQUIG, the interference pattern becomes more complex due to slight differences in the 'loop' sizes [79]. Similarly, the interference pattern from a superfluid grating structure increases its complexity as $\Delta\phi$ is increased. Although this degrades the dynamic range of the device, it gives rise to a unique by-product: sensitivity to absolute quantum phase differences. This interesting aspect is discussed in appendix E.
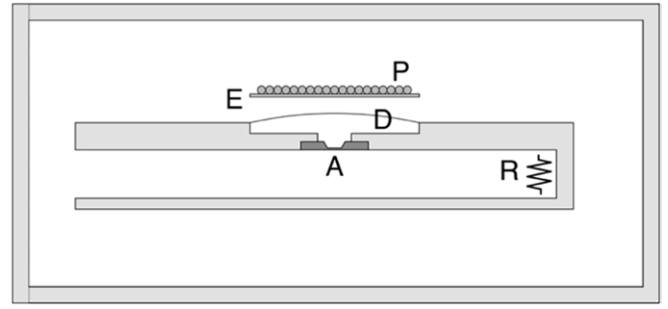
6.4. Single junction interference

The superfluid weak links described herein consist of an array of apertures rather than a single orifice. In experiments described thus far, an aperture array has behaved essentially as a single weak link with amplified overall mass current. Thus a main approach to superfluid interferometry has been having an array act as a single junction and using two or more arrays to interfere with each other. However, there is a different approach, which is to do interferometry with a single array by inducing phase differences between neighboring apertures. Collective coherent oscillations from individual aperture elements play a key role in such a scheme, and quantum interference from a single array has been demonstrated only recently in superfluid ^{4}He [80].

An experimental apparatus is schematically depicted in figure 27. Unshaded regions are filled with superfluid ^{4}He. An aperture array (labelled A) is configured as a part of a wall surface of a horizontal channel of cross-sectional area σ. A heat source (R) is placed at the closed end of this channel, and the fluid outside the channel behaves as a heat sink. The application of power to the heater generates a phase gradient along the channel: $\nabla\phi = (m/\hbar)(\rho_\mathrm{n}/\rho\rho_\mathrm{s}Ts\sigma)\dot{Q}$ as discussed in section 5.2. The resultant phase difference along the array of apertures allows the investigation of collective dynamics in a superfluid Josephson junction.

Figure 28 shows the measured Josephson mass-current oscillation amplitude as a function of heat input in the channel. The externally induced phase differences cause each column of apertures to oscillate with a fixed phase difference with respect to that of the adjacent columns. This is in close analogy to the characteristic of a diffraction grating. Combining all the mass currents leads to the grating-like modulation of the overall oscillation amplitude. The observed non-chaotic behavior implies that different apertures maintain temporal coherence of Josephson oscillations with a well-defined frequency of $\Delta\mu/h$ in the background of applied phase differences.

A silicon nitride film that contains the aperture array is installed with one of the array axes aligned with the heat current channel, and the device consists of $\sqrt{N}$ rows of $\sqrt{N}$ oscillators (each with oscillation amplitude I_0) with phase lags given by $\nabla\phi l$ where $l = 2\,\mu$m is the distance between the apertures. By
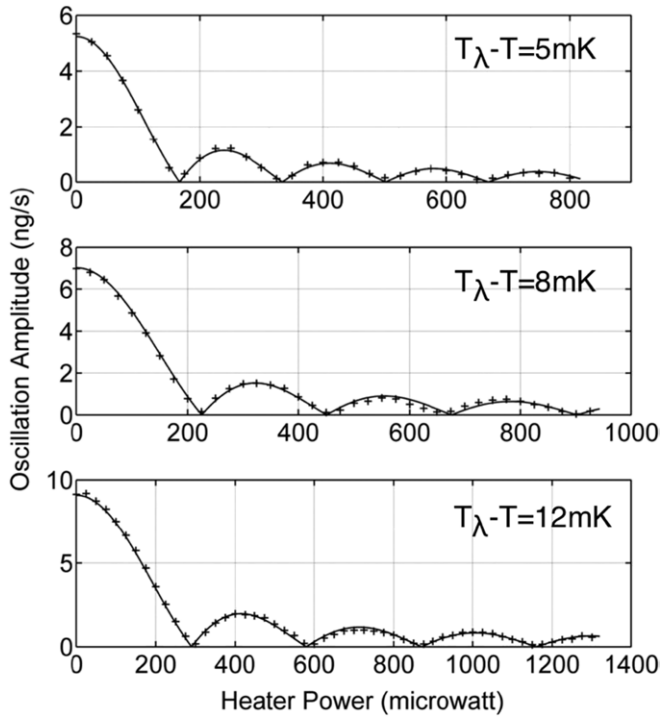
Figure 28. Mass-current oscillation amplitude versus heater power. The solid lines are fits, yielding $\sigma = 1.1, 1.1, 1.08 \times 10^{-5}\,\mathrm{m}^2$ for three different temperatures, which should be compared with the design value of $\sigma = 1.22 \times 10^{-5}\,\mathrm{m}^2$. Reprinted with permission from [80]. Copyright 2011 by the American Physical Society.

defining d to be the aperture diameter, the overall oscillation amplitude for the junction array can be written as [81]

$$\sqrt{N}\left|\frac{\sin(\Delta\phi_j/2)}{\Delta\phi_j/2}\right|\left|\frac{\sin(\sqrt{N}\Delta\phi_T/2)}{\sin(\Delta\phi_T/2)}\right|, \qquad (25)$$

where $\Delta\phi_j = \nabla\phi d$ is the phase shift contained in a single aperture and $\Delta\phi_T = \nabla\phi l$ is the phase shift between the neighboring apertures. We emphasize the close analogy with optical diffraction phenomena for many slit structures. The expected oscillation amplitudes as functions of $\dot{Q}$ have been fitted to the data and are shown in figure 28 as solid lines.

The superfluid experiment described here resembles that of the size effect investigation of the critical current in superconducting Josephson phenomena. In superconducting Josephson junctions, the critical current exhibits Fraunhofer patterns with magnetic field applied parallel to the junction [82, 83]. Viewing the superfluid aperture array as a web of a multi-junction interferometer, the system is also similar to granular superconducting thin film junctions and two- and three-dimensional superconducting Josephson junction arrays [84]. It may be possible to fabricate a longer array of apertures and utilize it in practical single junction interferometry in the future.

7. Future applications

We have already described how a SHeQUID may be used to monitor small changes in rotation rate (the Sagnac effect).
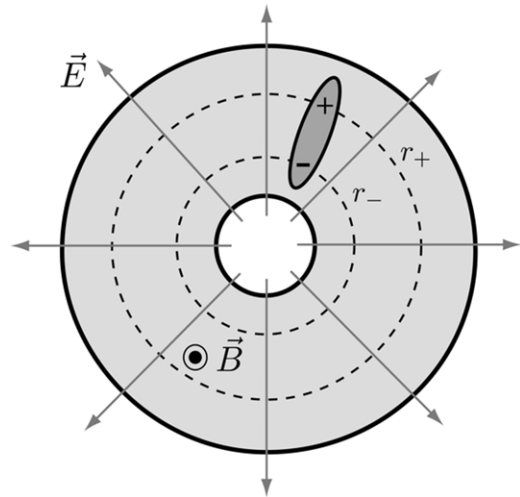

Figure 29. Quantum coherent matter is confined to a toroidal container that is positioned in a radial electric field and an axial magnetic field [88].

This may have applications in geodesy via monitoring small changes in the Earth's rotation rate. Such measurements are currently determined via very long baseline interferometry (VLBI) using an array of radio telescopes distributed across the globe. Optical Sagnac interferometers with enclosed area as large as $850\,\mathrm{m}^2$ are also employed for such measurements. It is also conceivable that a SHeQUID could be employed to observe the long sought frame dragging effect predicted by general relativity. However, any such measurement would probably have to be performed in a satellite to escape the much larger nuisance effects due to the Earth's rotation experienced by a SHeQUID positioned on the land.

We have also shown how the interferometer can be used to study the onset of quantum turbulence in superfluids. One naturally asks what other physical phenomena might be accessible with this novel device. In this section, we describe such a work in progress: an attempt to observe an Aharonov–Bohm (AB) effect in neutral quantum matter.

In 1959, Aharonov and Bohm predicted that electrons travelling outside a perfect solenoid would exhibit observable interference effects even though no classical force (but only a vector potential) exists in the spatial region traversed by the electrons [85]. Subsequent experiments proved the prediction to be correct [86]. In 1995, Wei *et al* predicted [87] a similar topological phase shift for neutral, nonpolar matter and suggested an experimental arrangement to test their prediction. The physical configuration involves neutral particles with no permanent electric dipole moment moving in a plane containing a radial electric field and a uniform magnetic field perpendicular to it. The applied electric field induces an electric dipole in the particles that then exhibit an AB phase shift. We briefly review this prediction and then describe a possible experiment in which a ^{4}He SHeQUID may be utilized to investigate the predicted phenomenon [88].

The existence of the AB phase shift in neutral matter can be seen by analyzing the situation shown in figure 29. For a wave packet of a particle of charge q moving around a perfect
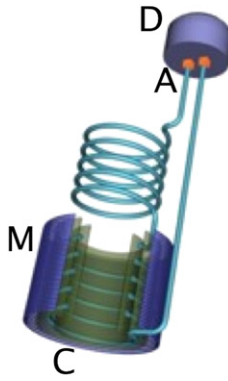
Figure 30. A possible experimental geometry [88]. A counter-wound helical interferometer loop is embedded within cylindrical capacitors (C) in the bore of a high field magnet (M). A diaphragm (D) is placed over two aperture arrays (A). Courtesy of A Joshi.

solenoid, the AB shift is given by

$$\Delta\phi_{AB} = \frac{q}{\hbar}\Phi, \tag{26}$$

where Φ is the magnetic flux contained within the solenoid.

The radial electric field shown in the figure 29 polarizes a neutral particle and induces an electric dipole. This dipole d can be thought of as a pair of equal and opposite charges q at distances r_+ and r_- with respect to the symmetry axis of the radial electric field: $d = q(r_+ - r_-)$. As these charges traverse closed circular paths (of radii r_+ and r_-) in a region where the magnetic field exists, they individually experience a shift in quantum phase according to (26). The phase shift for the positive charge is given by

$$\Delta\phi_+ = \frac{1}{\hbar} q B \pi r_+^2. \tag{27}$$

Similarly, the phase shift for the negative charge is

$$\Delta\phi_- = -\frac{1}{\hbar} q B \pi r_-^2. \tag{28}$$

The total phase shift, which is the sum of the two, can be written as $\Delta\phi = 2\pi B r d/\hbar$, where r is the radius of the particle's trajectory. The dipole moment induced by an electric field is $d = \alpha E$ where α is the particle's polarizability. If the radial electric field is created between concentric cylindrical electrodes (characterized by inner radius a and outer radius b) biased at potential difference V, $E = V/r ln(b/a)$ in cylindrical coordinates. The phase shift is then given by

$$\Delta\phi \approx \frac{2\pi \alpha B V}{\hbar ln(b/a)}. \tag{29}$$

As pointed out by Wei *et al*, if superfluid is the medium in the torus, since the phase gradient is related to particle velocity, the predicted phase difference above should correspond to a persistent superfluid current in the torus.

Figure 30 shows a possible apparatus configuration to observe the AB phase shift in neutral superfluid. The sensing loop of a SHeQUID plays the role of the torus depicted in figure 29. The loop in figure 30 contains two counter-wound parts to remove phase shifts caused by rotation-noise around the axis of the apparatus. Both halves of the loop are embedded in individual coaxial capacitors (only one set is shown). The outer cylindrical electrodes fit inside the bore of a superconducting magnet (parallel to the cylinder axis).

The polarizability of helium is 2×10^{-41} F m^2 [89]. For concentric cylinders with b/a ratio of 1.1, the predicted phase shift is $1.3 \times 10^{-5} BV$ rad. If the magnet generates 7 T and one applies 5 kV between the cylindrical electrodes, $\Delta\phi \sim 0.5$ rad for a single loop. By including approximately six turns in each half of the loop, the phase shift will be $\sim\pi$ thus sweeping out an entire cycle of the interference pattern. Seeing one complete interference cycle should make the most convincing test of the prediction.

There are some fundamental questions that may be clarified in this type of experiment. In the conventional description of AB effects, quantum wave packets traverse the two paths of an interferometer. It is the recombination of the packets that displays the interference. This is a valid picture for free-atom interferometers or electron beams used for AB type experiments, since in these instruments the particles, in a classical sense, actually do traverse the region where electromagnetic potentials exist. In contrast, in the superfluid ^{4}He interferometer, although the helium atoms very slowly drift due to the induced phase gradient, they do not physically traverse the interferometer path on the time scale of the measurement, which can be as short as a single Josephson oscillation cycle $\sim 10^{-3}$ s. Instead, the space filled with superfluid ^{4}He is described by a single macroscopic wavefunction with a phase that depends on time and space. All the atoms are in a single macroscopic entangled state, which is globally determined by the fields covering the region occupied by the fluid. The successful observation of the predicted phase shift in superfluid helium may suggest that the AB paradigm is more general than that needed to describe free particle propagation.

8. Accessibility of technology

The discovery of Josephson (and phase slip) oscillations at 2 K has moved the SHeQUID from a laboratory curiosity to a practical instrument. Commercial cryocoolers are now available that can maintain an appropriate temperature continuously without the need for the periodic transfer of liquid helium. Although cryocoolers have intrinsic vibration noise that may be difficult to eliminate, a properly designed dewar system without a cryocooler could maintain the required 2 K environment for at least one year.

With the continuous advancement in various lithography techniques and characterization tools, nanoscale aperture arrays necessary as weak-link elements are becoming easily accessible, even from commercial sources. Displacement transducers with 10^{-15} m Hz$^{-1/2}$ resolution (initially developed for gravity wave detection [18]) are also now well established using commercial SQUID systems. Thermometry with sub-nK resolution, originally developed for space-based fundamental

physics experiments [90], can be readily employed in Josephson work near T_λ for temperature stability [91]. These several developments permit any interested person to bring the power of the SHeQUID to bear on novel problems. One can even envision field instruments for geodesy or inertial navigation operating for long periods of time with little human intervention or cryogenic expertise.

At the time of this writing, the foremost hurdle to exploit the full resolution of a SHeQUID is environmental noise. This is certainly unfortunate, as experiments have shown that the device sensitivity is currently not close to any fundamental limitations, and various techniques are available to further enhance the intrinsic sensitivity. Superconducting SQUIDs can operate in a magnetically quiet environment using screened rooms and/or superconducting shielding. There are no such perfect shields for vibrational and rotational noise. Cryostat design that emphasizes rigidity and site positioning (e.g. in underground low vibration laboratories [92]) can go a long way to mitigate these nuisance background signals. Furthermore, the astatic coil configuration being developed for the AB experiment (figure 30) can help make the SHeQUID less susceptible to nuisance motion.

9. Conclusion

Josephson weak links between samples of macroscopic quantum systems such as superconductors, superfluids and Bose–Einstein condensates provide a unique tool with which to explore quantum mechanics and an opportunity for applications based on macroscopic quantum physics. Starting with the ^{3}He Josephson work in the millikelvin regime and accelerated by the discovery of ^{4}He weak-link physics near 2 K, various physical phenomena such as Josephson oscillations, phase slip oscillations, the Fiske effect, Shapiro effect, plasma mode and dynamical bifurcation have been observed. Many of these unique phenomena have now been quantified and utilized to construct superfluid quantum interference devices as well as to significantly enhance their intrinsic sensitivity for both fundamental and applied sciences. A new field of research has emerged wherein the superfluid interferometer can be used not only to study the quantum properties of superfluid helium but also to probe some aspects of fundamental physics that have heretofore remained elusive. We hope that readers of this review will be able to understand the SHeQUID principles and relevant technology.

Fascinating phenomena continue to be discovered in the field of macroscopic quantum physics, and analogies between the phenomena presented here and those in superconductors and Bose–Einstein condensates also point the way toward investigations of similar effects in other quantum systems.

Appendix A. Transition from strongly coupled to weakly coupled quantum fluids

The system depicted in figure 7 is adequate to observe both Josephson oscillations in the weakly coupled regime and phase slip oscillations in the strongly coupled regime. Since the coupling is determined by the ratio of aperture size d to the temperature dependent healing length ξ_4, the system can be brought from one limit to the other by varying the temperature.

Figures A1 and A2 show sections of two flow transients excited by the application of a voltage-induced pressure step across the array of apertures. The time traces show the displacement of the diaphragm as the fluid is driven through the apertures under the influence of a time-dependent chemical potential gradient. In figure A1, $\xi_4/d = 0.4$. The regularly spaced slope discontinuities in the first half of the plot are the signatures of phase slips that occur whenever the accelerating flow reaches a critical velocity v_c. By contrast, in figure A2, $\xi_4/d = 1.8$ and the system is in the Josephson weak-link regime. The sharp phase slip discontinuities have been smoothed out into sinusoidal Josephson oscillations. The $\Delta\mu$ induced by the initial pressure step relaxes to equilibrium throughout each transient. When $\Delta\mu$ reaches 0, quantum oscillations (Josephson or phase slip oscillations) cease, and lower frequency oscillations proceed due to interplay of the fluid inertia in the channel and the restoring force of
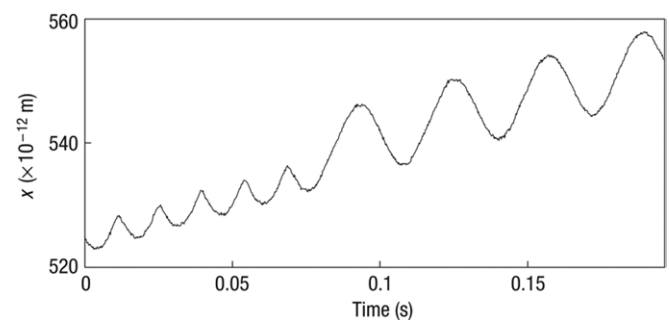

Figure A1. Diaphragm position versus time. Cusps in the first half of the transient are the phase slips that display a sudden reversal of flow. $T_\lambda - T = 7.4$ mK. Reprinted by permission from Macmillan Publishers Ltd: *Nature Phys.* [94], copyright 2006.
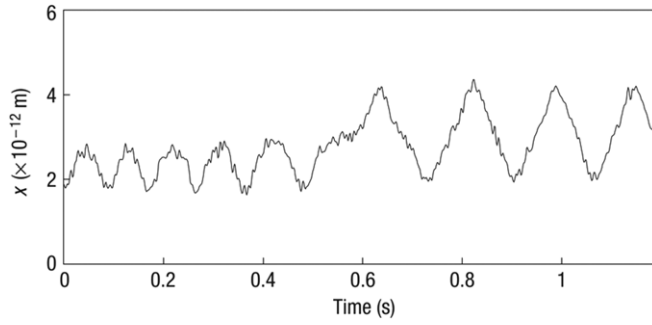
Figure A2. Diaphragm position versus time. Near $t = 0.6$ s where the Josephson oscillations decay into the plasma mode oscillations, $\Delta\phi$ approaches a local maximum of just less than π. The current $I \propto dx/dt$ slows here, reflecting the sinusoidal nature of $I_s(\Delta\phi)$. $T_\lambda - T = 0.8$ mK. Reprinted by permission from Macmillan Publishers Ltd: *Nature Phys.* [94], copyright 2006.
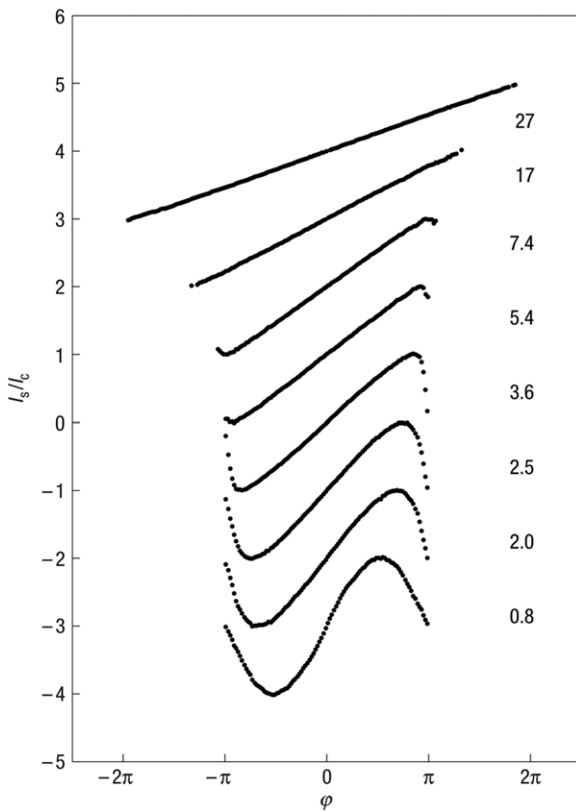

Figure A3. Evolution of current–phase relation. The corresponding $T_\lambda - T$ is indicated in millikelvin to the right of each curve. Each curve has been normalized by its maximum value I_c and shifted vertically. Reprinted by permission from Macmillan Publishers Ltd: *Nature Phys.* [94], copyright 2006.

the diaphragm. These are called the plasma mode (or the Helmholtz mode) oscillations and can be seen as the larger displacement oscillations in the second halves of figures A1 and A2.

The dynamics of coupled quantum liquids is determined by the current–phase relation $I_s(\Delta\phi)$. Superfluid current is proportional to superfluid velocity, which, by (2), is proportional to the phase gradient, which itself is proportional to $\Delta\phi$. Therefore, for the strongly coupled channel, $I_s(\Delta\phi)$ should be a linear function. By contrast, in a weakly coupled
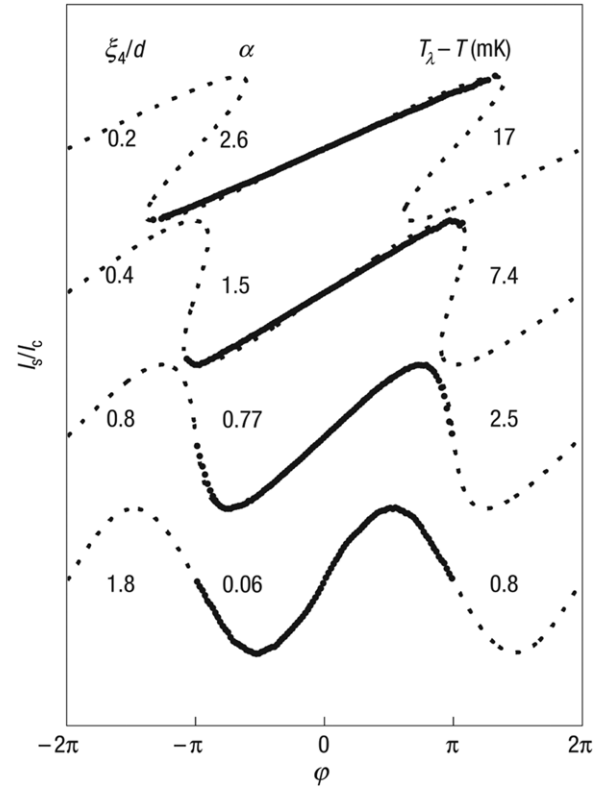

Figure A4. Fits to normalized current–phase relation using the Deaver–Pierce model. Reprinted by permission from Macmillan Publishers Ltd: *Nature Phys.* [94], copyright 2006.

regime, $I_s(\Delta\phi)$ should be sinusoidal as governed by the Josephson equation (9).

The general method for extracting current–phase relation from ^{4}He flow data is conceptually similar to that used by Backhaus *et al* for a ^{3}He system [93]. From transients such as those shown in figures A1 and A2, the current $I(t)$ is determined by differentiating the displacement $x(t)$. The phase difference across the apertures, $\Delta\phi(t)$, is determined by integrating the phase-evolution equation (10), with the phase offset determined by the fact that $\Delta\phi = 0$ when $I_s = 0$. Elimination of the common variable t between $I_s(t)$ and $\Delta\phi(t)$ yields the current–phase relation $I_s(\Delta\phi)$.

The measured current–phase functions for several different temperatures are shown in figure A3 [94]. The values shown within the plot are $T_\lambda - T$ in mK. A smooth transformation occurs from the low-temperature strong-coupling regime where $I_s(\Delta\phi)$ is linear into the weak-coupling regime, where $I_s(\Delta\phi)$ morphs into a sine function.

The measured $I_s(\Delta\phi)$ is well described by an empirical model (mentioned in section 3.4) consisting of a linear kinetic inductance in series with a purely sinusoidal one. The model prediction is plotted in figure A4 for four different temperatures along with the actual measured $I_s(\Delta\phi)$. The striking agreement lends insight into how the evolution of $I_s(\Delta\phi)$ can be viewed as the transition from a multiple-valued hysteretic function to one that is single valued.

We have shown in section 5 that both types of oscillations (Josephson and phase slips) can be used to construct superfluid quantum interference devices. The significant feature for such

devices is that the oscillations have a well-defined frequency, and that the entire sample of superfluid remains quantum coherent throughout.

We note that the current–phase relation for a superfluid ^{3}He system shows a more complicated evolution with bi-stability and π states (without phase slips), and the Deaver–Pierce parameterization is found to not always work [95–97]. We leave the detailed discussion to [19].

Appendix B. Array synchronicity

In this appendix we briefly discuss why all the individual apertures within an array might oscillate synchronously: i.e. in phase. One of the main reasons why the observation of ^{4}He Josephson phenomena in an array of apertures/slits was a surprise is that thermal fluctuations were thought to destroy the temporal phase coherence in a given aperture as well as spatial coherence (synchronicity) among the array.

In a single weak link, the observation of temporally coherent Josephson phenomena requires $E_J \gg k_B T$, where E_J is the Josephson energy arising from the spatial overlap of the wavefunctions [9]. Zimmermann has argued that, for a single weak link in superfluid ^{4}He, $E_J < k_B T$ near T_λ [98].

For treating spatial phase coherence in a weak-link array, one can consider an array of apertures spaced D apart from each other. For a slab of superfluid with area D^2 and thickness τ, one can equate the kinetic energy in that volume $\frac{1}{2}\rho_s D^2 \tau v_s^2$ to thermal energy $\frac{1}{2}kT$. Using (2), phase fluctuation due to thermal energy can then be written as

$$\Delta\phi_{\text{fluc}} \sim \frac{m}{\hbar}\sqrt{\frac{kT}{\tau\rho_s}}. \tag{B1}$$

For a superfluid ^{3}He system at its associated temperature of 1 mK, $\tau \sim 100\,\mu$m gives $\Delta\phi_{\text{fluc}} \sim 2 \times 10^{-4}$ rad, which is small enough that spatial phase coherence (i.e. synchronous behavior) may be expected for a ^{3}He nanoaperture array. In contrast, $\sqrt{T/\rho_s}$ is 3–4 orders of magnitude larger for a ^{4}He system near 2 K. Therefore, this simple line of argument would suggest that spatial phase coherence might not prevail for a ^{4}He Josephson system near T_λ.

Although temporal coherence in a given aperture and spatial phase coherence in an array of apertures are both expected to be compromised by thermal fluctuations in superfluid ^{4}He, ^{4}He Josephson oscillations have been observed for aperture arrays. Furthermore, measurement of the oscillation amplitude indicates that the overall oscillation from an array of N apertures is roughly N times that which is expected for a single aperture deep in a Josephson regime.

In a phase slip regime, phase slips which occur simultaneously closer to T_λ seem to lose their simultaneity as the temperature is lowered [99, 100]. In figure B1, the measured phase slip oscillation amplitude is plotted as a function of temperature along with the expected value for a fully synchronous case (estimated from a measured current–phase relation). Close to T_λ, where phase slip oscillation starts to morph into Josephson oscillation, the oscillations are found to be synchronous. That behavior
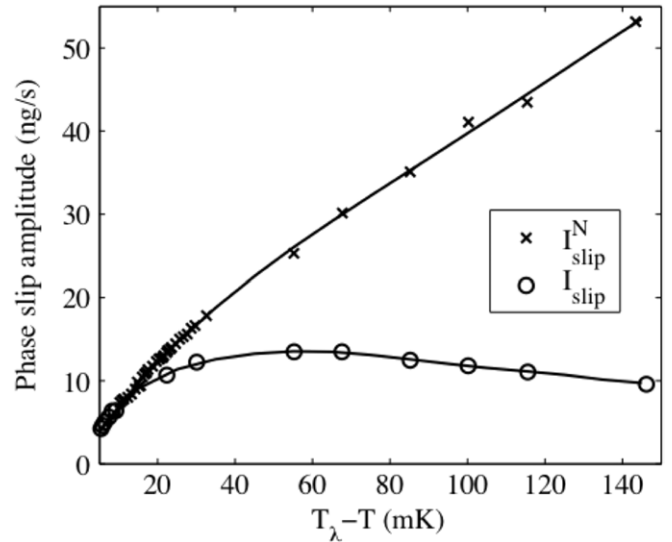

Figure B1. Phase slip oscillation amplitude versus temperature. Circles show the measured values, and crosses indicate the expected values for a fully synchronous case. Reprinted with permission from [99]. Copyright 2006 by the American Physical Society.

weakens considerably as the temperature is lowered, a fact that discourages using lower temperatures to boost the oscillation amplitude. Several attempts have been made to explain this unexpected temperature dependence.

Chui *et al* have presented a thermodynamic treatment of a superfluid Josephson junction in the Josephson regime [101]. By rigidly locking N junctions in parallel, they argue that the overall fluctuations should be suppressed by a factor of $\sqrt{N}$, a result consistent with the observation of Josephson oscillation in an array of junctions even though E_J may be less than $k_B T$ for a single junction at 2 K.

For the lower temperature phase slip regime, Pekker *et al* have presented a model that couples all the apertures through the bulk superfluid allowing one to investigate how the critical velocity distribution among various apertures affects the experimental observables [102]. The results that they obtain with a mean-field approximation and numerical analysis for a small number of apertures capture the general experimental findings.

One possible mechanism for the observed loss of synchronicity at lower temperatures may involve variations in the surface microstructure among the array of apertures. With the fluid flowing fastest near asperities, the critical velocity for an aperture must be affected by the surface structure. Since the superfluid healing length is a function of temperature, how much of these nanoscale inhomogeneities the fluid actually 'sees' should depend on temperature as well. The healing length decreases from $\sim$10 to $\sim$1.5 nm as the temperature is lowered from $T_\lambda - T \approx 10$ mK to $T_\lambda - T \approx 160$ mK. If the surface variations are on the order of a few nanometers, this could very well provide a critical velocity distribution whose width increases with decreasing temperature while allowing the individual apertures to maintain well-defined periodic oscillations.

At this time, the variation in apparent critical current reflected in figure B1 remains a profound mystery, and more

work is required to find an explanation. If future understanding leads to designs wherein the oscillation amplitude continues to increase as temperature is decreased, one can hope to make even more sensitive devices based on the Josephson oscillations. However, there is a 'silver lining' to figure B1. As we have shown, SHeQUIDs exhibit changes in oscillation amplitude due to some external phase shifting phenomenon. Temperature also changes the oscillation amplitude, and these experiments near T_λ typically require a high-resolution thermometer [90, 91] as a feedback element to achieve the necessary temperature stability. The temperature independent plateau existing near $T_\lambda - T \sim 60$ mK lets one relax the required temperature stability of the SHeQUID, thus rendering the technology more accessible to the experimentalist.

Appendix C. Bifurcation: Josephson parametric amplification

As demonstrated with the Fiske amplification, nonlinear dynamics can be taken advantage of in various ways to achieve signal enhancement. In this appendix, we discuss another nonlinear phenomenon, bifurcation, and its possible application as an amplifier. Consider the apparatus depicted in figure 7. In an ideal weak-coupling limit, an aperture array coupled to a spring-like diaphragm behaves as a nonlinear oscillator. One can parametrize the junction with a nonlinear hydrodynamic inductance $L_J = (\kappa/2\pi)(\mathrm{d}I/\mathrm{d}\phi)^{-1} = \kappa/(2\pi I_c \cos\phi)$.

The junction inductance is shunted in parallel by a hydrodynamic capacitance C associated with the presence of a diaphragm and heat capacity and compressibility of the fluid that it displaces. The combined system is an LC oscillator with the dynamics described by a phase particle with coordinate ϕ in a so-called washboard potential $U = (\kappa I_c/2\pi)(1 - \cos\phi)$ [9]. The oscillation within this potential well is referred to as the plasma mode, and its natural frequency $\omega_p = 1/\sqrt{L_J C}$ is called the plasma frequency. One can also view the system as a rigid pendulum with the phase difference ϕ playing the role of the pendulum's displacement angle. One of the simplest models for such a system is a damped, forced oscillator with a cubic nonlinearity [103]: $\ddot{x} + \gamma\dot{x} + \alpha x + \beta x^3 = B\cos(\omega_d t)$, where B is the driving parameter, ω_d is the drive frequency, and γ, α and β represent the strengths of damping, stiffness and nonlinearity, respectively. This is the so-called Duffing oscillator model with a soft spring condition ($\beta < 0$) [104, 105]. The expected oscillator response is plotted as a function of detuning parameter $2Q(\omega_d/\omega_0 - 1)$ in figure C1 for increasing values of the dimensionless driving amplitude $f \equiv \sqrt{\beta/\alpha^3}$.

For small driving strength, the sinusoidal potential is well approximated by a parabola, and therefore the particle behavior is harmonic with its Lorentzian response. However, for large amplitude oscillations, nonlinear terms act to reduce the oscillation frequency, causing the peak to bend toward the left. For even stronger drives, the bending of the peak becomes so much that the oscillator bifurcates from a single valued to a bistable regime. At locations such as the one indicated by a vertical line in figure C1, the system can have
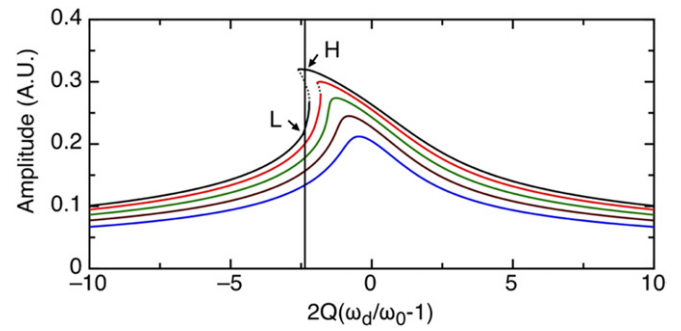

Figure C1. Predicted bifurcation behavior for increasing drive levels. Reprinted with permission from [106]. Copyright 2010 by the American Physical Society.
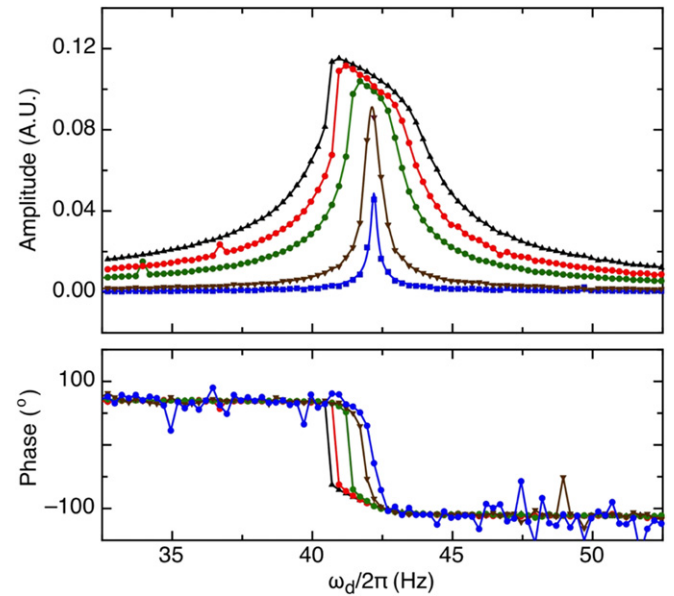

Figure C2. Amplitude of plasma oscillation and oscillation phase relative to the drive. Reprinted with permission from [106]. Copyright 2010 by the American Physical Society.

two possible oscillation states with different amplitudes and phases. Increasing the oscillation amplitude at such bias points eventually causes the system to switch between the two dynamical states (from point L to point H, for example), giving rise to a sharp step on the lower frequency side of the distorted peak.

Nonlinear bifurcation has been observed for a superfluid ^{4}He Josephson junction [106]. The apparatus used is similar to the one shown in figure 7 with a weak link formed by a 75×75 array of 60 nm apertures. The diaphragm is driven at frequency ω_d and the amplitude of superfluid plasma oscillations as well as oscillation phase relative to the drive is recorded. Figure C2 is an example of such data, while sweeping the drive frequency ω_d. When the drive is kept minimal, both amplitude and phase plots show behavior expected for a linear resonant system. However, as the excitation is increased to push the system into a nonlinear regime, the resonant peak bends toward lower frequency as predicted, and an abrupt step appears on the left side of the peak as the system bifurcates and transitions from one state to another. This effect is also pronounced in the phase plot where a smooth zero-crossing evolves to an

abrupt switching between two oscillation states as the drive is increased.

This bifurcation could form a basis for signal amplification, in close analogy with rf-driven Josephson bifurcation amplifiers currently utilized in quantum computing research [107]. As long as the system remains in the Josephson regime, the Josephson oscillation amplitude and plasma frequency are related as $\omega_p^2 \propto I_c$, and a signal from small change in ω_p will be enhanced greatly at the bifurcation point. Therefore, the bifurcation phenomenon itself becomes a sensitive threshold detector for the change in Josephson oscillation amplitude. Applied to a SHeQUID, the system could act as a sensitive switch for a change in the quantum mechanical phase that appears in the superfluid loop. The Josephson current-phase characteristic in ^{4}He exists very close to T_λ, a regime where the small value of ρ_s substantially reduces I_c. Using smaller apertures and employing larger numbers of them may allow one to utilize bifurcation phenomena at lower temperatures without having to lose any signal size.

Appendix D. Interferometer size limitations

A sensitive device is only as good as the noise environment. For the data shown in figure 24, the phase noise from the environment is already about four times higher than the smallest phase change that the device is capable of detecting if only limited by electronic noise. One may be able to use an astatic sense loop configuration to make the device more independent of rotational/vibrational noise from the surroundings. With these environmental limitations in mind, we mention some techniques that can be used to enhance the SHeQUID beyond that already achieved.

All the phase shifts induced by external fields are proportional to the length of the SHeQUID loop, and one might imagine making ever larger devices to take advantage of that feature. However there is a limit to such size increase. Analogous to superconducting weak links, a superfluid weak-link kinetic inductance is given by $L = (\kappa/2\pi)(\mathrm{d}\phi/\mathrm{d}I)$. In the weak-link limit near zero phase difference, this becomes $L_J = \kappa/2\pi I_c$. A simple tube of length l has a kinetic inductance given by $L_t = l/\rho_s\sigma$ where σ is the tube's cross-sectional area. If the length of the torus becomes too large, the loop inductance dominates the array inductance and the external phase shift is appreciably reduced along the tube rather than the apertures. This decreases the modulation depth of the interference pattern, diminishing its sensitivity. Probably the best compromise is for the loop inductance to match the array inductance. This sets a lower limit on the tube's internal radius which can be estimated to be $r_{\min} \approx \sqrt{dlN}$ where d is the aperture diameter and N the number of apertures. With this estimate, an interferometer with loop circumference ∼1 m requires a tube radius of ∼1 cm. It is unknown at this time if the SHeQUID can be scaled to these (and even larger) dimensions. A superfluid interferometer with 53 cm path length and 225 cm^2 sensing area in counter-wound reciprocal geometry has been recently developed [108].

The Josephson mass-current oscillation of magnitude I_c gives rise to velocity oscillations of the diaphragm. With the technology used thus far, the diaphragm's displacement amplitude is detected. For a sinusoidal fixed amplitude mass current, the displacement scales inversely with the frequency. On the other hand, operating at higher frequencies will in principle increase the signal to noise due to a higher sampling rate. If a sensitive velocity transducer is employed instead of a displacement transducer, one could operate at much higher Josephson frequencies. This may help not only in investigating more robust resonant features at higher frequencies for Fiske amplification (away from low frequency building noises) but also in reducing the response time in the flux-lock mode of operation, allowing reliable measurements of phase changes that occur in a much shorter time scale.

Appendix E. Absolute gauge for quantum mechanical phase differences

SHeQUIDs provide researchers with a novel method to probe aspects of fundamental physics by registering changes in phase difference. However, a measurement of "absolute" phase difference has always remained elusive. We emphasize that double-path interferometers monitor changes in phase shift $\Delta\phi$. When the devices are turned on, there can already be some phase shift, either from external influences or from trapped vortices. Such initial phase offset, $\Delta\phi_0$, cannot be determined because the two-slit pattern is 2π periodic and thus physically indistinguishable from $\Delta\phi_0 \pm 2\pi n$. Having a means to measure absolute phase difference (i.e. without the modulo $2\pi n$) between two locations in quantum coherent matter could be important in understanding the nature of quantum phase and the quantum mechanics that governs it. This situation may be remedied with an asymmetric quantum interference grating.

We have discussed the grating interferometer in section 6.3. To make an absolute $\Delta\phi$ gauge, one may utilize a grating structure but with purposefully designed geometrical asymmetry. For example, this can be achieved by varying the areas enclosed by the multiple loops present in the grating. This approach has been taken with superconducting SQUIDs to make absolute measurements of small magnetic field [109, 110]. These true magnetometers utilize varying enclosed areas in the SQUID array to achieve magnetic flux to electric current transfer function that is not 2π periodic.

In a similar manner, a SHeQUID with area variations results in phase to mass-current transfer function that is not 2π periodic. This effect can be seen in the four-slit superfluid quantum interference grating discussed in section 6.3. The interference pattern at low $\Delta\phi$ values is shown in figure 26, and its evolution (increasing complexity with increasing $\Delta\phi$) can be seen in figure E1. In designing that particular experiment, care was taken to minimize any geometrical differences. However, the finite width of four phase probing pipes introduced finite asymmetry, giving rise to the changing shape of the modulation pattern.

By balancing the dynamic range and the degree of change required per period in an interference pattern, a device could be optimized and used as an absolute measure for quantum phase shift. In practice, an asymmetric grating interferometer may have some advantages since their performance is not
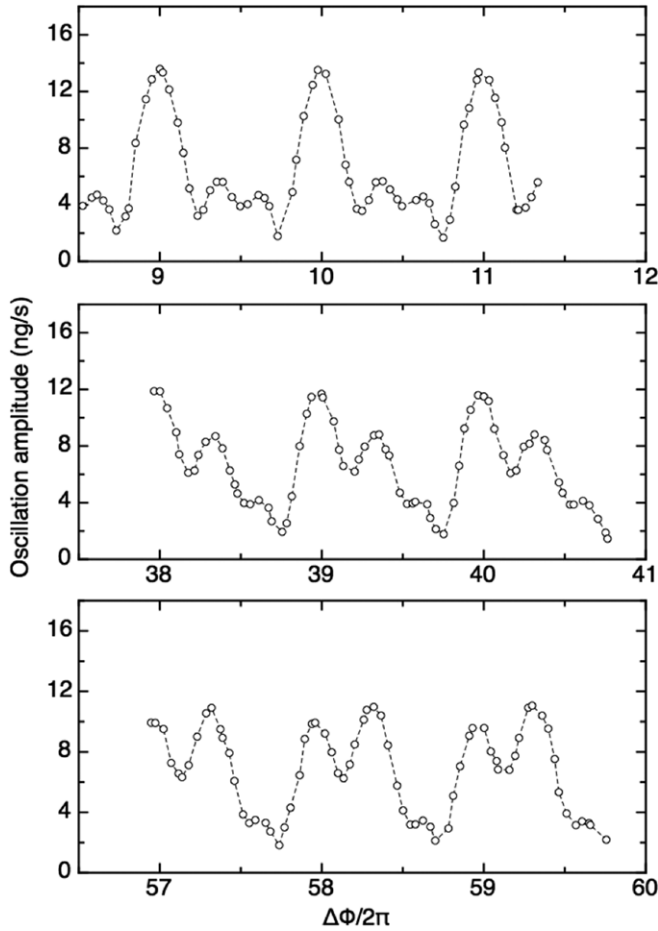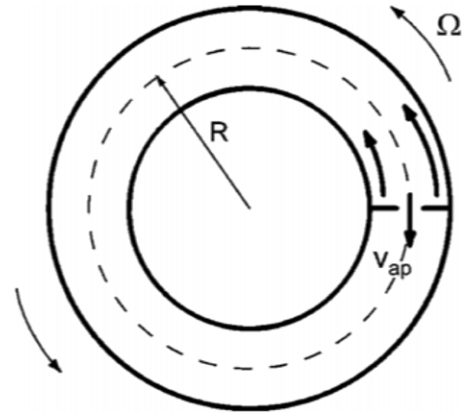
Figure F1. Superfluid-filled torus, partitioned by a wall containing a small aperture. Reprinted with permission from [115]. Copyright 2003, American Institute of Physics.

Figure E1. Interference patterns for large $\Delta\phi$ for a four-slit interferometer. Reprinted with permission from [78]. Copyright 2008 by the American Physical Society.

degraded by spreads in the Josephson junction parameters (as mentioned in section 6.3) or deviations in the loop sizes. One can argue that their performances as absolute gauges rely on such differences instead. Developed further, this type of superfluid device could provide insights to equilibrium state and non-equilibrium dynamics of phase coherent quantum matter and may become useful for researchers investigating Kibble–Zurek scenarios [111, 112] of formation of topological defects, where a knowledge of absolute phase difference can play a crucial role.

Appendix F. Related devices: superfluid gyrometers

The quantum interference devices described thus far are built upon the principle that matter waves from multiple junctions interfere with relative phase shifts determined by external influences. Although they might not technically fit this category, there have been other superfluid devices that work as rotation sensors. To differentiate from dc-SQUID type interference devices and for historical reasons, we call these devices gyrometers. We briefly discuss two such examples.

Consider a toroidal container, partitioned by a wall containing a small aperture (depicted in figure F1). When the torus is made to rotate at an angular velocity Ω, the

moving partition forces the fluid in the body of the torus to go into a solid body motion. The phase integral condition ($\oint \nabla\phi \cdot \mathrm{d}l = 2\pi n$) for a closed path that threads the aperture and the arms of the torus gives the phase difference across the orifice $\Delta\phi = -4\pi\vec{\Omega} \cdot \vec{A}/\kappa$, where A is the area spanned by the torus. This phase difference corresponds to the induced superfluid backflow in the aperture to cancel the solid body flow contributions. Using (2), the rotation-induced velocity in the aperture can be written as $v_{\mathrm{ap}} = -2\vec{\Omega} \cdot \vec{A}/l_{\mathrm{eff}}$, where l_{eff} is the effective hydrodynamic length of the aperture. Since the torus area A is macroscopic while the aperture length l_{eff} is microscopic, the device behaves as a rotational velocity amplifier. This rotation-induced velocity [113] was first measured [114] by Avenel and Varoquaux with a ^{4}He apparatus depicted in figure F2. The basic structure is similar to their double-hole resonator apparatus shown in figure 3, but the orifice is now connected to the parallel channel through a two-turn pickup loop, forming the equivalent of a torus with an effective area of $4\,\mathrm{cm}^2$. An orifice is a $0.17 \times 2.8\,\mu\mathrm{m}^2$ slit in a $0.2\,\mu\mathrm{m}$ thick Ni foil. As described in the ^{4}He phase slip section (section 4.1), the Saclay team drove the soft membrane with a sinusoidal force at the resonant frequency of the oscillator, ramping up the amplitude and eventually driving phase slips in succession. The amplitude of the membrane at which the phase slips occur is directly proportional to the critical velocity. However, the observed critical velocity in the orifice is now shifted by the rotation-induced backflow $v_{\mathrm{ap}} = -2\vec{\Omega} \cdot \vec{A}/l_{\mathrm{eff}}$. Therefore, the critical velocity measurement becomes a rotation sensing method in this configuration. Such data are shown in figure F3. Modulation in the critical velocity is seen as the apparatus is reoriented in the lab frame, capturing different amount of rotation flux from the spinning Earth. This experiment was carried out with superfluid ^{4}He at $T \sim 12\,\mathrm{mK}$. An experiment with better accuracy has been reported by the same authors [47], and independent corroboration has been provided by Schwab et al [46]. Later work by Bruckner and Packard [115] employed a sensing area two orders of magnitude larger than the work of Schwab et al, leading to $3 \times 10^{-6}\,\mathrm{rad\,s^{-1}\,Hz^{-1/2}}$ sensitivity at $T \sim 300\,\mathrm{mK}$. Further increase of the pickup area and hence the sensitivity enhancement (without introducing extra intrinsic noise) is
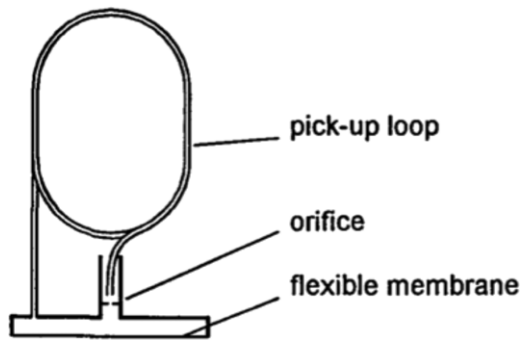
Figure F2. Gyrometer schematic. A weak link is shunted by a long parallel tube. The closed path through the weak link and the tube has sufficient enclosed area that reorientation of the cell in the Earth's rotational field creates phase shifts. Reprinted with permission from [114]. Copyright 1996, Springer.
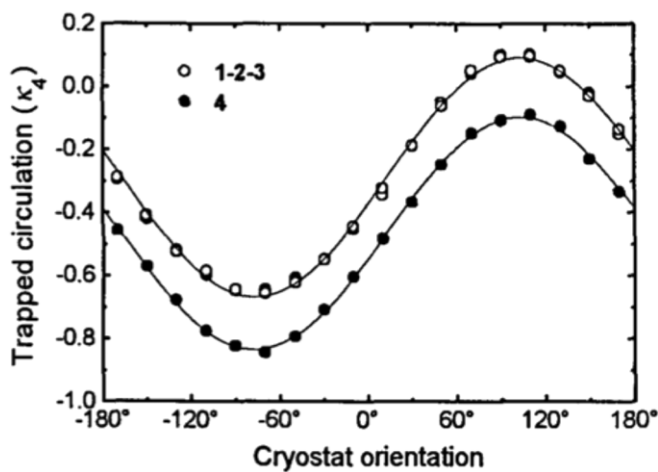

Figure F3. Velocity circulation as a function of apparatus orientation about vertical. Reprinted with permission from [114]. Copyright 1996, Springer.

reported to be feasible. We note that phase slip gyrometers discussed above are in the form of an rf-SQUID [2], where a loop of quantum coherent matter is interrupted by a single junction. However, the Josephson relation (9) is not essential for these devices to work as their operation principle is based on phase slip phenomena.

An example of rf-SQUID type gyrometers that make use of the Josephson relation is the single junction ^{3}He gyro reported by Mukharsky *et al* [48]. The device is very similar to the one shown in figure F2, but it is operated with superfluid ^{3}He in the Josephson regime below 1 mK. The weak link is an array of 198 80 nm holes with 2 μm spacing fabricated in a 100 nm thick SiN window. For a nonlinear current–phase relation, a weak-link inductance is a function of the phase difference. Since the phase difference is now a function of rotation flux (i.e. $\Delta\phi = -4\pi\vec{\Omega} \cdot \vec{A}/\kappa$), resonant frequency changes can be used to read the amount of rotation captured in the pickup loop. Resonant frequency as a function of rotation flux is shown in figure F4. From the power spectrum of the noise, the authors deduce the sensitivity of this ^{3}He gyrometer to be 1.4×10^{-7} rad s^{-1} Hz$^{-1/2}$.

We note that one of the main differences between these single junction devices and multi-junction devices described
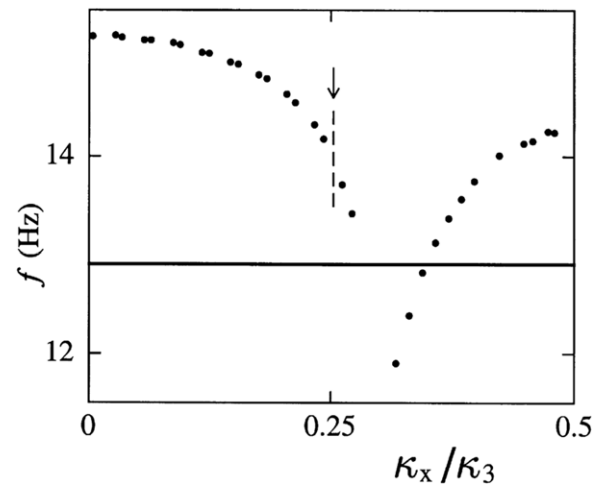

Figure F4. Resonant frequency versus rotation flux. Reprinted from [48], copyright 1992 by Elsevier.

in earlier sections is the acquisition rate. In superfluid gyrometers (rf-SQUID equivalent), the acquisition rate is typically $\sim$10 Hz, limited by their natural resonant frequency. For dc-SQUID-like superfluid devices, the acquisition rate can be three orders of magnitude higher as it is only limited by Josephson frequency. On the other hand, the inductance of the rf-SQUID type devices (and thus the loop area) can be made larger than that of the dc-SQUID type devices. Therefore, the comparison of the 'ultimate' performances of these devices is a rather complex issue. See a review on gyrometers by Avenel *et al* [116].

Appendix G. Atom and laser interferometers

As mentioned in section 5.1, gyroscopes based on Sagnac interferometry have been employed with light as well as atoms. A rotation with an angular velocity $\vec{\Omega}$ induces a shift in the interference fringe by amount $\Delta\phi = 4\pi m\vec{A} \cdot \vec{\Omega}/h$, where $\vec{A}$ is the area vector of the interferometer loop, and m is the mass of the interfering particle. Because of the large mass, the Sagnac phase with the same area A is much larger for neutral atoms than it is for photons. For example, comparing cesium atoms with a HeNe laser, the same amount of rotation should cause $\sim$6 $\times$ 10^{10} times larger phase shifts for atom interferometers compared with photons. On the other hand, light interferometers gain advantage by the much larger sensing areas made possible by high finesse mirrors. The G ring laser in the underground laboratory of the Geodetic Observatory in Wettzell [92] has, for example, a sensing area of 16 m^2, leading to a rotation sensitivity of 1.5×10^{-10} rad s^{-1} Hz$^{-1/2}$.

For atom interferometers, which typically enclose areas on the order of tens of mm^2 [43], the limitation for increasing the effective sensing area often comes from the lack of better beam splitters. It is also difficult to employ curved geometry in atom interferometry due to dispersive coupling of motion between the guide direction and confining direction in curved atomic waveguides [117]. Rather than transporting atoms in a curved guide, a scheme to move a straight waveguide while enclosing an area in a folded figure 8 configuration has been

recently demonstrated [118]. In the case of superfluid helium quantum interference devices, curved geometry is not an issue since the whole volume within the guide is occupied by the fluid that is macroscopically quantum coherent. However, the limitation for increasing the sensing area comes from increased hydrodynamic inductance associated with the longer loop [108]. Although one may be able to increase the cross-sectional area of the tube to compensate for the increase in the loop length, such configurations have not been systematically tested and it is not clear how the significant increase in overall fluid volume will affect the device performance. We note that a scheme to transfer rotation flux from a longer pickup loop to a coupled neutral interferometer loop has been suggested recently by Golobashkin *et al* for superfluid quantum interference devices [119, 120]. The feasibility of such a scheme is not clear to us at the time of this writing and needs to be investigated in more detail.

We refer readers to [42, 43, 92] for details on the short-term sensitivity and long-term stability of atom and laser interferometers. Recently, Josephson effects have been observed in BECs [121, 122], opening up an exciting possibility for constructing a unique quantum interference device with coherent clouds of atoms similar to the ones described in this review.

References

[1] Josephson B D 1962 *Phys. Lett.* **1** 251
[2] Clarke J and Braginski A I 2004 *The SQUID Handbook: Fundamentals and Technology of SQUIDs and SQUID Systems* (Weinheim: Wiley)
[3] Tilley D R and Tilley J 1990 *Superfluidity and Superconductivity* (Bristol: Institute of Physics Publishing)
[4] Landau L D and Lifshitz E M 1987 *Fluid Mechanics* (New York: Pergamon)
[5] Feynman R P, Leighton R B and Sands M L 1963 *The Feynman Lectures in Physics* vol 3 (Reading, MA: Addison-Wesley)
[6] Kittel C 1996 *Introduction to Solid State Physics* (New York: Wiley)
[7] Anderson P W 1966 *Rev. Mod. Phys.* **38** 298
[8] Packard R E 1998 *Rev. Mod. Phys.* **70** 641
[9] Likharev K K 1986 *Dynamics of Josephson Junctions and Circuits* (New York: Academic)
[10] Dayem A H and Grimes C C 1966 *Appl. Phys. Lett.* **9** 47
[11] Vollhardt D and Wolfle P 1990 *The Superfluid Phases of Helium-3* (New York: Taylor and Francis)
[12] Avenel O and Varoquaux E 1988 *Phys. Rev. Lett.* **60** 416
[13] Henkel R P, Smith E N and Reppy J D 1969 *Phys. Rev. Lett.* **23** 1276
[14] Sukhatme K, Mukharsky Y, Chui T and Pearson D 2001 *Nature* **411** 280
[15] Hoskinson E, Parckard R E and Haard T 2005 *Nature* **433** 376
[16] Pereversev S V, Loshak A, Backhaus S, Davis J C and Packard R E 1997 *Nature* **388** 449
[17] Avenel O and Varoquaux E 1985 *Phys. Rev. Lett.* **55** 2704
[18] Paik H J 1976 *J. Appl. Phys.* **47** 1168
[19] Davis J C and Packard R E 2002 *Rev. Mod. Phys.* **74** 741
[20] Deaver B S and Pierce J M 1972 *Phys. Lett.* A **38** 81
[21] Varoquaux E, Avenel O, Ihas G and Salmelin R 1992 *Physica* B **178** 309
[22] Amar A, Lozes R L, Sasaki Y, Davis J C and Packard R E 1993 *J. Vac. Sci. Technol.* B **11** 259
[23] Simmonds R, Marchenkov A, Vitale S, Davis J C and Packard R E 2000 *Phys. Rev. Lett.* **84** 6062
[24] Penanen K and Chui T 2004 *APS March Meeting (Montreal)* L15.007
[25] Hoskinson E and Packard R E 2005 *Phys. Rev. Lett.* **94** 155303
[26] Hoskinson E 2005 *PhD Thesis* University of California at Berkeley
[27] Onsagar L 1949 *Nuovo Cimento* **6** 249
[28] Feynman R P 1955 *Progress on Low Temperature Physics* vol 1, ed C J Gorter (Amsterdam: North-Holland) chapter 2
[29] Anderson P W 1966 *Quantum Fluids* ed D F Brewer (Amsterdam: North-Holland) p 146
[30] Hess G B 1971 *Phys. Rev. Lett.* **27** 977
[31] Varoquaux E, Avenel O and Meisel M W 1987 *Can. J. Phys.* **65** 1377
[32] Zimmermann W 1996 *Contemp. Phys.* **37** 219
[33] Amar A, Sasaki Y, Lozes R, Davis J C and Packard R E 1992 *Phys. Rev. Lett.* **68** 2624
[34] Langer J S and Fisher M E 1967 *Phys. Rev. Lett.* **19** 560
[35] Steinhauer J, Schwab K, Mukharsky Y, Davis J C and Packard R E 1995 *Phys. Rev. Lett.* **74** 5056
[36] Steinhauer J, Backhaus S and Packard R E 1995 *Phys. Rev. B* **52** 9654
[37] Burkhart S, Bernard M, Avenel O and Varoquaux E 1994 *Phys. Rev. Lett.* **72** 380
[38] Varoquaux E, Meisel M W and Avenel O 1986 *Phys. Rev. Lett.* **57** 2291
[39] Post E J 1967 *Rev. Mod. Phys.* **39** 475
[40] Stedman G E 1997 *Rep. Prog. Phys.* **60** 615
[41] Werner S A, Staudenmann J L and Colella R 1979 *Phys. Rev. Lett.* **42** 1103
[42] Gustavson T L, Landragin A and Kasevich M A 2000 *Class. Quantum Grav.* **17** 2385
[43] Durfee D S, Shaham Y K and Kasevich M A 2006 *Phys. Rev. Lett.* **97** 240801
[44] Keith D W, Ekstrom C R, Turchette Q A and Pritchard D E 1991 *Phys. Rev. Lett.* **66** 2693
[45] Simmonds R W, Marchenkov A, Hoskinson E, Davis J C and Packard R E 2001 *Nature* **412** 55
[46] Schwab K, Bruckner N and Packard R E 1997 *Nature* **386** 585
[47] Avenel O, Hakonen P and Varoquaux E 1997 *Phys. Rev. Lett.* **78** 3602
[48] Mukharsky Y, Avenel O and Varoquaux E 2000 *Physica* B **284** 287
[49] Hoskinson E, Sato Y and Packard R E 2006 *Phys. Rev. B* **74** 100509(R)
[50] Chui T and Penanen K 2005 *Phys. Rev. B* **71** 132509
[51] Schreiber K U, Velikoseltsev V, Rothacher M, Klugel T, Stedman G E and Wiltshire D L 2004 *J. Geophys. Res.* **109** B06405
[52] London F 1950 *Superfluids* (New York: Wiley)
[53] Sato Y, Joshi A and Packard R E 2007 *Phys. Rev. Lett.* **98** 195302
[54] Sato Y, Joshi A and Packard R E 2007 *Appl. Phys. Lett.* **91** 074107
[55] Zheng X, Jianye L, Wei Z, Baozhang S and Feng M 2010 *IEEE Position Location and Navigation Symp. (Indian Wells, CA)* 10.1109/PLANS.2010.5507136
[56] Glaberson W I and Donnelly R J 1966 *Phys. Rev.* **141** 208
[57] Schwarz K W 1990 *Phys. Rev. Lett.* **64** 1130
[58] Vinen W F and Donnelly R J 2007 *Phys. Today* **60** 43
[59] Sato Y, Joshi A and Packard R E 2007 *Phys. Rev. B* **76** 052505
[60] Day P K, Moeur W A, McCready S S, Sergatskov D A, Liu F C and Duncan R V 1998 *Phys. Rev. Lett.* **81** 2474
[61] Haussmann R and Dohm V 1991 *Phys. Rev. Lett.* **67** 3404
[62] Donnelly R J 1991 *Quantized Vortices in Helium 2* (New York: Cambridge University Press)
[63] Donnelly R J 2001 *Quantized Vortex Dynamics and Superfluid Turbulence* ed C F Barenghi *et al* (Berlin: Springer)
[64] Donnelly R J 1965 *Phys. Rev. Lett.* **14** 39

[65] Bewley G P, Lathrop D P and Sreenivasan K R 2006 *Nature* **441** 588
[66] Guo W, Cahn S B, Nikkel J A, Vinen W F and McKinsey D N 2010 *Phys. Rev. Lett.* **105** 045301
[67] Backhaus S and Packard R E 1996 *Czech. J. Phys.* **46** 2743
[68] Hoskinson E, Sato Y, Penanen K and Packard R E 2006 *AIP Proc.* **850** 119
[69] Sato Y 2010 *Phys. Rev.* B **81** 172502
[70] Coon D D and Fiske M D 1965 *Phys. Rev.* **138** A744
[71] Simmonds R W, Loshak A, Marchenkov A, Backhaus S, Pereversev S, Vitale S, Davis J C and Packard R E 1998 *Phys. Rev. Lett.* **81** 1247
[72] Riehle F, Kisters T, Witte A, Helmcke J and Borde C J 1991 *Phys. Rev. Lett.* **67** 177
[73] Gustavson T L, Bouyer P and Kasevich M A 1997 *Phys. Rev. Lett.* **78** 2046
[74] Berman P R 1997 *Atom Interferometry* (New York: Academic)
[75] Zimmerman J E and Silver A 1966 *Phys. Rev.* **141** 367
[76] Th A, De Waele A M, Kraan W H and De Bruyn Ouboter R 1968 *Physica* **40** 302
[77] Jeng J T, Huang K H, Wu C H, Chen K L, Chen J C and Yang H C 2007 *IEEE Trans. Appl. Supercond.* **17** 691
[78] Sato Y, Joshi A and Packard R E 2008 *Phys. Rev. Lett.* **101** 085302
[79] Oppenlander J 2003 *Advances in Solid State Physics* vol 43, ed B Kramer (Berlin: Springer) p 731
[80] Narayana S and Sato Y 2011 *Phys. Rev. Lett.* **106** 055302
[81] Barone A and Paterno G 1982 *Physics and Applications of the Josephson Effect* (New York: Wiley)
[82] Jaklevic R C, Lambe J and Silver A H 1964 *Phys. Rev. Lett.* **12** 159
[83] Rowell J M 1963 *Phys. Rev. Lett.* **11** 200
[84] Fazio R and van der Zant H 2001 *Phys. Rep.* **355** 235
[85] Aharonov Y and Bohm D 1959 *Phys. Rev.* **115** 485
[86] Chambers R G 1960 *Phys. Rev. Lett.* **5** 3
[87] Wei H, Han R and Wei X 1994 *Phys. Rev. Lett.* **75** 2071
[88] Sato Y and Packard R E 2009 *J. Phys.: Conf. Ser.* **150** 032093
[89] Pobell F 1996 *Matter and Methods at Low Temperatures* (Berlin: Springer)
[90] Welander P B and Hahn I 2001 *Rev. Sci. Instrum.* **72** 3600
[91] Narayana S and Sato Y 2010 *IEEE Trans. Appl. Supercond.* **20** 2402
[92] Schreiber K U, Klugel T, Velikoseltsev A, Schlutter W, Stedman G E and Wells J P R 2009 *Pure Appl. Geophys.* **166** 1485
[93] Backhaus S, Pereverzev S, Loshak A, Davis J C and Packard R E 1997 *Science* **278** 1435
[94] Hoskinson E, Sato Y, Hahn I and Packard R E 2006 *Nature Phys.* **2** 23
[95] Marchenkov A, Simmonds R W, Backhaus S, Loshak A, Davis J C and Packard R E 1999 *Phys. Rev. Lett.* **83** 3860
[96] Backhaus S, Pereverzev S, Simmonds R W, Loshak A, Davis J C and Packard R E 1999 *Nature* **392** 687
[97] Avenel O, Mukharsky Y and Varoquaux E 2000 *Physica* B **280** 130
[98] Zimmermann W 1987 *Proc. 5th Oregon Conference on Liquid Helium* p 118
[99] Sato Y, Hoskinson E and Packard R E 2006 *Phys. Rev.* B **74** 144502
[100] Sato Y, Hoskinson E and Packard R E 2007 *J. Low Temp. Phys.* **149** 222
[101] Chui T, Holmes W and Penanen K 2003 *Phys. Rev. Lett.* **90** 085301
[102] Pekker D, Barankov R and Goldbart P M 2007 *Phys. Rev. Lett.* **98** 175301
[103] Wiesenfeld K and McNamara B 1985 *Phys. Rev. Lett.* **55** 13
[104] Landau L D and Lifshitz E M 1988 *Course of Theoretical Physics: Mechanics* (Oxford: Pergamon)
[105] Nayfeh A H and Mook D T 1979 *Nonlinear Oscillations* (New York: Wiley)
[106] Narayana S and Sato Y 2010 *Phys. Rev. Lett.* **105** 205302
[107] Siddiqi I, Vijay R, Pierre F, Wilson C M, Metcalfe M, Rigetti C, Frunzio L and Devoret M H 2004 *Phys. Rev. Lett.* **93** 207002
[108] Narayana S and Sato Y 2011 *Phys. Rev. Lett.* **106** 255301
[109] Oppenlander J, Haussler C and Schopohl N 2001 *Phys. Rev.* B **63** 24511
[110] Caputo P, Tomes J, Oppenlander J, Haussler C, Friesch A, Trauble T and Schopohl N 2005 *IEEE Trans. Appl. Supercond.* **15** 1044
[111] Zurek W H 1985 *Nature* **317** 505
[112] Maniv A, Polturak E and Koren G 2003 *Phys. Rev. Lett.* **91** 197001
[113] Aarts R, Ihas G, Avenel O and Varoquaux E 1994 *Physica* B **194** 493
[114] Avenel O and Varoquaux E 1996 *Czech. J. Phys.* **46** 3319
[115] Bruckner N and Packard R E 2003 *J. Appl. Phys.* **93** 1798
[116] Avenel O, Mukharsky Y and Varoquaux E 2004 *J. Low Temp. Phys.* **135** 745
[117] Murch K W, Moore K L, Gupta S and Stamper-Kurn D M 2006 *Phys. Rev. Lett.* **96** 013202
[118] Wu S, Su E and Prentiss M 2007 *Phys. Rev. Lett.* **99** 173201
[119] Golovashkin A I, Izmailov G N, Ozolin V V, Tskhovrebov A M and Zherikhina L N 2010 *Grav. Cosmol.* **16** 78
[120] Golovashkin A I, Zherikhina L N, Tskhovrebov A M, Izmailov G N and Ozolin V V 2010 *JETP* **111** 332
[121] Albiez M, Gati R, Folling J, Hunsmann S, Cristiani M and Oberthaler M K 2005 *Phys. Rev. Lett.* **95** 010402
[122] Levy S, Lahoud E, Shomroni I and Steinhauer J 2007 *Nature* **449** 579